RSC Advances

PAPER

View Article Online
View Journal | View Issue

Cite this: *RSC Adv.*, 2025, **15**, 29335

Tailoring electronic and optoelectronic properties of 2D-SiC *via* defects and doping: a first-principles study toward efficient white light-emitting diodes

Md. Mahfuzul Haque [ab] and Sajid Muhaimin Choudhury *[a]

The advent of graphene catalyzed extensive exploration into two-dimensional (2D) materials, owing to their extraordinary electronic, mechanical, and optical properties. Among these, two-dimensional silicon carbide (2D-SiC) has emerged as a compelling candidate for next-generation optoelectronic devices due to its inherent planar structure, robust mechanical strength, high exciton binding energy, high thermal stability, and wide band gap. In this work, we present a comprehensive first-principles investigation into the effects of intrinsic point defects including vacancies and antisites as well as substitutional doping with various single foreign atom (*e.g.*, As, Bi, Ga, Ge, In, P, Pb, Sb, Sn, Te, Ca, K, Mg) on the electronic and optical properties of 2D-SiC. Using density functional theory (DFT), we demonstrate that the direct band gap of pristine 2D-SiC is preserved in the presence of key defect types and dopants, affirming its suitability for efficient light-emitting applications. Building upon these findings, we propose a novel light-emitting diode (LED) architecture utilizing defect, doping-tailored 2D-SiC as the active emissive layer. Simulated optical and electrical performance metrics, including power spectral density, current–voltage characteristics, luminous power, light extraction efficiency, and CIE color coordinates, confirm the feasibility of achieving high-performance white light emission through strategic RGB color mixing. These findings confirm the capabilities of defect and dopant-engineered 2D-SiC as a high-performance material platform for adjustable light emission within the visible spectrum, which highlights its appropriateness for incorporation into cutting-edge optoelectronic devices and solid-state lighting applications.

Received 27th June 2025
Accepted 13th August 2025

DOI: 10.1039/d5ra04586j

rsc.li/rsc-advances

1 Introduction

The extraction of a single graphene layer from graphite in 2004[1] marked a significant milestone in materials science, sparking a surge of interest in the exploration of additional two-dimensional (2D) materials. These fundamentally thin materials have attracted significant interest due to their remarkable physical, optical, and electronic properties.[2–5] 2D materials are highly desirable for next-generation technologies due to their exceptional characteristics, which make them ideal for applications in flexible electronics, nanoelectronics, and optoelectronics.[6–10] The unique features of these materials, such as lower scattering rates of charge carriers, improved carrier mobility, and higher conductivity, make them more effective than bulk silicon in the operation of electronic devices, which is fundamental to the modern semiconductor industry.[11,12] Despite graphene's remarkable properties, its intrinsic zero band gap remains a fundamental drawback for its use in nanoelectronics applications.[13] For a two-dimensional material to be viable in electronic devices, the presence of a finite and tunable band gap is crucial. To mitigate this constraint, many ways have been investigated to produce a band gap in graphene. Various strategies have been explored, including chemical doping, application of in-plane strain, surface functionalization (*e.g.*, hydrogenation), and molecular adsorption.[14–22] In a research, Denis *et al.*[23] demonstrated that the incorporation of substitutional impurities including aluminum, silicon, phosphorus, and sulfur into monolayer and bilayer graphene may successfully induce a band gap.

A promising method involves substituting alternate carbon atoms in graphene's hexagonal lattice with silicon atoms, forming a two-dimensional silicon carbide (2D-SiC) monolayer. This structure retains a planar form and demonstrates a band gap of around 2.557 eV, as forecasted by density functional theory (DFT) calculations employing the generalized gradient approximation with the Perdew–Burke–Ernzerhof (GGA-PBE) functional.[24] The emergence of the band gap is attributed to the difference in electronegativity between Si and C, which induces partial ionic character in the otherwise covalent bonding network. Moreover, the dynamic stability of the 2D-SiC has been repeatedly confirmed using phonon dispersion and

[a]*Department of Electrical and Electronic Engineering, Bangladesh University of Engineering and Technology, Dhaka, 1205, Bangladesh. E-mail: sajid@eee.buet.ac.bd*
[b]*Department of Electrical and Electronic Engineering, Jamalpur Science and Technology University, Jamalpur, 2012, Bangladesh. E-mail: mahfuzul@jstu.ac.bd*

associated analysis in several theoretical studies.[24–28] A planar SiC monolayer is generated by sp^2 hybridization between Si and C atoms, in contrast to the sp^3 hybridization observed in bulk SiC phase.[29,30] Theoretical investigations have validated that ultrathin wurtzite structures, including SiC, BeO, GaN, ZnO, and AlN thin films, are capable of undergoing phase change (from sp^3 to sp^2) while maintaining stability. Freeman *et al.*[31] reported that materials such as SiC and ZnO tend to favor a graphitic-like configuration when reduced to just a few atomic layers, as this structure becomes the most energetically favorable in the ultrathin limit. This theoretical insight was subsequently validated through experimental work on ultrathin films of ZnO, AlN, and MgO.[32–39] The dimensional transition from bulk to monolayer leads to a contraction of the Si–C bond length from about 1.89 Å to 1.79 Å, while the bond angle increases from 109° to 120°.[30,40,41] This alteration reflects the planar hexagonal lattice structure typical of two-dimensional materials. The decrease in dimensionality and the onset of quantum confinement effects lead to unique electronic and optical properties in monolayer SiC, positioning it as an intriguing option for cutting-edge nano-electronic and optoelectronic applications.[42–44] Moreover, 2D SiC has been documented to demonstrate remarkable mechanical strength, positioning it among the stiffest two-dimensional materials following graphene and hexagonal boron nitride.[45] The wide band gap, combined with excellent thermal and mechanical properties, renders monolayer SiC especially appealing for applications in high-power and high-temperature electronic devices.[46]

2D-SiC has gotten a lot of attention as a possible base for nano-electronic and optoelectronic devices because it is very thermally stable, strong, has a wide bandgap, and allows carriers to move easily. So far, most theoretical investigations have focused on the electrical and optical properties of monolayer 2D-SiC. Singh *et al.*[47] used HSE06 simulations to get very accurate measurements of the electrical and optical characteristics of pristine monolayer SiC. Recent advancements have been achieved in the synthesis of two-dimensional SiC structures within the experimental domain. Lin *et al.*[48] effectively created quasi-two-dimensional SiC flakes with thicknesses under 10 nm by facilitating a reactive interaction between silicon quantum dots and graphene. Despite the quasi-2D-SiC flakes not being atomically thin, the authors noted alterations in the electrical structure indicated of quantum confinement. Further advancement was achieved by Chabi *et al.*,[49] who utilized a catalyst-free carbothermal reduction method to produce 2D-SiC nanoflakes with average lateral dimensions around 2 μm and thicknesses reduced to approximately 2–3 nm, corresponding to about seven to ten atomic layers. Yang *et al.*[50] used the chemical vapor deposition (CVD) approach to create multi-layer 2D-SiC films and ultra-thin 2D-SiC layers (8–10 nm thick). Through the use of a wet exfoliation technique, Chabi *et al.* were able to successfully revive 2D-SiC from hexagonal SiC.[29] A recent study by Polley *et al.*[51] highlighted the successful growth of a large-area, atomically thin epitaxial monolayer of SiC featuring a honeycomb lattice using the "bottom-up" solid state fabrication technique. The findings indicate that, in contrast to numerous other 2D materials that experience environmental instability, this experimentally synthesized 2D-SiC monolayer exhibits environmental stability and remains intact at room temperature. At the same time, there have been significant improvements in defect and dopant engineering, as well as the integration of several types of 2D materials for optoelectronic uses including light-emitting devices.[52–55] The results show that the configurations studied in this study can be used in real life, and they also give a good reason for more theoretical research on 2D-SiC-based LED.

Ion implantation is a well-established and precise technique widely used for doping in semiconductor materials. This approach involves the acceleration and precise direction of dopant ions into the host lattice, specifically two-dimensional silicon carbide, facilitating meticulous placement at designated lattice sites.[56] The concentration and distribution of dopants can be precisely controlled through ion implantation, a recognized technique for selective doping in semiconductors. The introduction of dopant precursors during the development phase of CVD enables the generation of doped two-dimensional SiC layers.[44,57,58] This method not only proves to be optimal for large-scale manufacturing but also facilitates uniform doping throughout the process.

Defects such as dopants, vacancies, antisites, and interstitials are recognized for their essential influence in substantially modifying the electronic and optical properties of 2D materials. The significant quantum confinement in two-dimensional systems leads to a notable difference in the interaction between defected and host wave functions compared to what is seen in bulk three-dimensional materials. He *et al.*[59] and Bezi Javan[60] looked at how isolated point defects and light-element dopants like nitrogen and boron affect magnetic characteristics and localized electronic states. There hasn't been enough research on how different types of intrinsic defects, like vacancies and antisites, and a variety of substitutional dopants affect the optical transitions and emission properties of 2D-SiC. This study presents a thorough first-principles examination of the electronic, and optical characteristics associated with different defect types in a monolayer of SiC. Utilizing first principle DFT, we conduct a thorough examination of the impacts of intrinsic point defects, including vacancies and antisites, alongside substitutional doping with foreign atoms such arsenic (As), bismuth (Bi), gallium (Ga), germanium (Ge), indium (In), phosphorus (P), lead (Pb), antimony (Sb), tin (Sn), tellurium (Te), calcium (Ca), potassium (K), and magnesium (Mg). In addition, we explore more complex defect configurations involving coupled defect types, such as vacancy-dopant and antisite-vacancy pairs. This thorough examination provides important insights into the impact of different defects on the electronic and optical properties of 2D-SiC, emphasizing its potential for advanced device applications like light-emitting diodes (LEDs). A foundational objective of this study is to evaluate how vacancy and anti-site defects, along with substitutional doping, affect the band structure of 2D-SiC. Determining monolayers that maintain a direct band gap through these modifications is essential for efficient photon emission, which is a necessary condition for LED technology. Based on

our findings, a novel LED architecture is proposed where defect-modified 2D-SiC acts as the primary emissive layer.

2D-SiC, a lot of work has been done on other two-dimensional materials, such as transition metal dichalcogenides (TMDs), black phosphorus (BP), and 2D perovskites, to make light-emitting technologies for the next generation.[61–63] These materials have changeable optical bandgaps, strong excitonic effects, and high quantum efficiencies. Yu *et al.*[64] showed that localized strain fields could be used to precisely tune the spectra of single-photon emitters in WSe_2 monolayers. However, these strain-engineering methods often need complicated fabrication processes, which limits their ability to be used in larger integrated devices. Sheng *et al.*[65] showed that using high-quality CVD-grown 2D materials, they made an asymmetric structure of monolayer WS_2. This structure made red-light-emitting LEDs that worked well and could be seen glowing under both forward and reverse bias. This method shows that optoelectronic platforms based on 2D materials are becoming more and more possible.

Defect and doping engineering are a scalable and stable way to change the emission properties of 2D semiconductors. Point defects, such as vacancies and grain boundaries, can make mid-gap states and change the paths that radiative recombination takes.[66,67] Controlled addition of point defects to vertical heterostructures has been shown to improve out-of-plane charge transport, which in turn improves interlayer exciton dynamics and optoelectronic performance.[68] Adding components like nitrogen or aluminum to a material can change its band structure and carrier concentration in a way that improves charge injection and transport in light-emitting devices.[66,67] Recent improvements in photo-induced doping make it possible to change the type and density of carriers, which makes optoelectronic systems based on 2D materials more flexible.[69]

Graphene and TMDs are 2D materials that are used as functional interlayers and dopants in real-world LED designs like OLEDs, QLEDs, and PeLEDs. These materials make it easier for charges to enter, change work functions, and stop excitons from dying, which all make devices last longer and work better.[70] Even if the results in several two-dimensional systems are promising, 2D-SiC has not been fully studied for emission tuning and white-light generation using systematic defect or doping procedures.

Earlier simulation endeavors, including those conducted by Islam *et al.* showed effective blue light emission through the development of a 2D-SiC-based multi-quantum well structure utilizing SILVACO TCAD tools.[71] The design utilized 4H-SiC as the quantum barrier and GaN as the electron-blocking layer, aiming to improve carrier confinement and recombination efficiency. In a similar vein, Rashid *et al.* introduced an LED model that incorporates 4H-SiC and 6H-SiC layers, assessing performance metrics including luminous power, current–voltage behavior, and spectral characteristics under different structural conditions.[72] Expanding upon these established frameworks, we employed monolayer pure 2D-SiC, defected 2D-SiC, and doped 2D-SiC as active layers in the proposed LED to determine their emission characteristics within the visible red, green, and blue spectrum. This study uses first-principles DFT calculations and TCAD-based device modeling to look at how inherent point defects and substitutional doping affect the optoelectronic properties of monolayer 2D-SiC. This work looks at different types of intrinsic point defects and different types of substitutional point dopants in a systematic way to figure out how they change the electronic band structure and optical absorption properties. Through a color mixing approach, we proposed that integrating these individual red, green, and blue LEDs into a single chip could enable white light emission. This design shows that defect- and dopant-engineered 2D-SiC can be used as a tunable, stable, and scalable base for future solid-state lighting applications. Furthermore, we analyzed the power spectral density, light extraction efficiency, luminous power, CIE chromaticity coordinates, and current–voltage characteristics of the proposed LED, providing comprehensive insight into its optical and electrical performance.

2 Methodology

2.1 Computational method

In this study, we investigated the optical and electrical properties of 2D-SiC under pristine, defect-induced, and doped conditions using first-principles-DFT method in conjunction with a norm-conserving pseudopotential.[73,74] The Perdew–Burke–Ernzerhof (PBE) functional within the generalized gradient approximation (GGA)[75,76] framework was used to describe the exchange–correlation interactions the computations were conducted using the simulation software Quantum Espresso.[77] The data input consisted of several crucial initial configurations, including charge cut-off energy, Brillouin zone grid, lattice constants, crystal topologies, and kinetic energy. In the process of optimizing the structure, a Monkhorst–Pack grid with dimensions of $8 \times 8 \times 1$ is employed. Furthermore, electronic properties are calculated by sampling the Brillouin zone using a k-grid of $16 \times 16 \times 1$.[78] The kinetic energy cut-off for the plane-wave basis set was set to 400 Ry. Atomic relaxation continued until the residual forces on each atom were less than 0.01 eV $Å^{-1}$ and the threshold for convergence for the total energy is set at 1.0×10–6 eV.[79] The complex dielectric function was calculated to determine the absorption characteristics of the material, including peak wavelengths in the visible range. The optical properties were determined using a Monkhorst–Pack k-mesh grid with size of $8 \times 8 \times 1$.[78,80] The $4 \times 4 \times 1$ supercell of the 2D SiC monolayer were built using periodic boundary conditions, as shown in Fig. 1(a). A total of 32 atoms were utilized to include various materials dopants, antisite defects, double vacancy defects, or single vacancy defects in the 2D SiC monolayer. In investigations of defects in two-dimensional materials, the supercell size is often used because it strikes a good balance between the cost of computing and the ability to mimic localized point defects while reducing artificial interactions.[47,57,81]

We used the GGA-PBE functional and the independent-particle approximation to figure out the optical properties, which include the imaginary part of the dielectric function and the absorption spectra. It is well known that GGA functionals usually underestimate bandgaps and leave out interactions

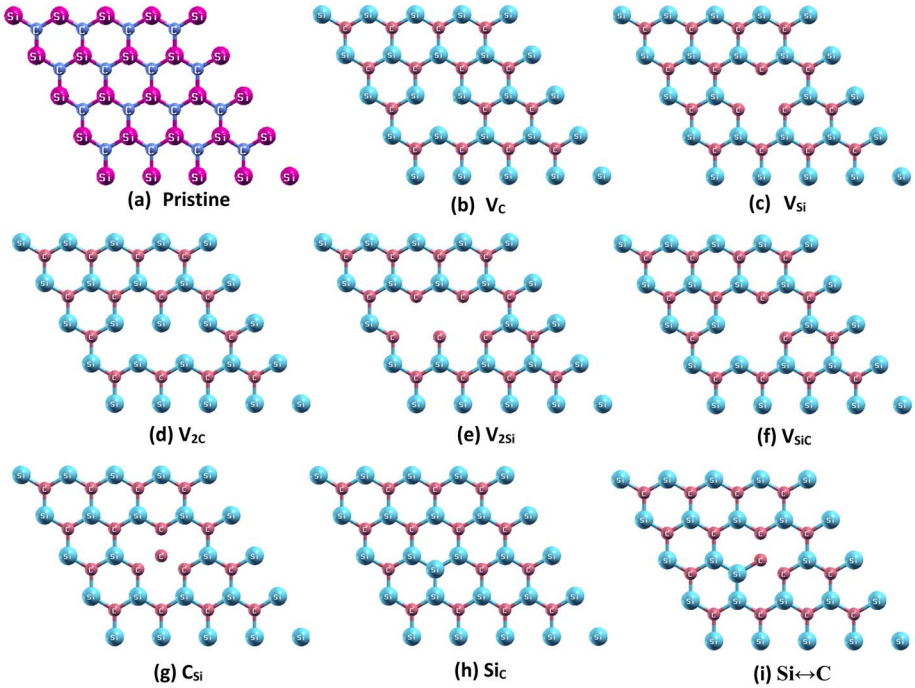

Fig. 1 (a) The structural configuration of pristine monolayer SiC; the structural configuration of single vacancy defect in a monolayer of SiC: (b) V_C, (c) V_{Si}; the structural configuration of double vacancy defect in a monolayer of SiC: (d) V_{2C}, (e) V_{2Si}, (f) V_{SiC}; the structural configuration of antisite defect in a monolayer of SiC: (g) C_{Si}, (h) Si_C, (i) Si ↔ C.

between electrons and holes. This method is a useful and reliable way to test a lot of different point defect and dopant setups. The bandgap for pristine 2D-SiC was found to be 2.57 eV, which is in line with the experimental results reported by Polley *et al.*[51] and with the results of earlier theoretical investigations that used hybrid functionals.[47] This constancy comes from a balancing act: the PBE's underestimating of the bandgap is offset by the fact that excitonic binding is not included in the optical spectra. This makes the absorption onset a good estimate. Using GW+BSE or hybrid functionals with time-dependent DFT to make more precise computations would give better estimates of excitonic transitions, radiative lifetimes, and optical sensitivity.

The GGA-PBE functional was also used in this study to look at the electrical characteristics of both pristine and modified 2D-SiC. The estimated bandgap for pristine monolayer 2D-SiC is 2.57 eV, which is quite close to what was found in experiments[51,82,83] and supports earlier hybrid functional calculations.[47] This agreement confirms that the procedure is consistent and supports its usage for systematically looking at different point defect and dopant setups. The band structure of pristine 2D-SiC, determined using HSE06, is presented in the electrical results section.

This work looks at how intrinsic point defects and substitutional dopants affect 2D-SiC. All of the defect and dopant configurations were put in on purpose to make the situations seem authentic. Engineering materials at the atomic level is a common way to improve the properties of semiconductors for use in optoelectronic applications.[84–86] The choice of point defects and dopants is based on theory and backed up by experiments.[87–92] We looked at intrinsic defects including silicon vacancy (V_{Si}), carbon vacancy (V_C), silicon–carbon divacancy (V_{SiC}), and antisite defects like Si_C, C_{Si}, and Si ↔ C. Defects in SiC often happen when it grows in a non-stoichiometric way, when it is ion irradiated, when it is thermally annealed, or when it is treated with plasma. Existence has been shown to be present in bulk and two-dimensional SiC systems, affecting electronic structure, trap states, and radiative recombination, as shown in previous research.[93,94] Point defects can also be intentionally introduced to tailor the electrical and optical properties of the material.

A single carbon vacancy, denoted as V_C, was introduced into the monolayer SiC structure by removing one carbon atom, as illustrated in Fig. 1(b). Similarly, a silicon vacancy (V_{Si}) was created by removing a single Si atom from the lattice, as shown in Fig. 1(c). To investigate more complex defect structures, two types of double vacancies were also considered. The removal of two carbon atoms resulted in the formation of a double carbon vacancy, V_{2C} (Fig. 1(d)), while the removal of two silicon atoms produced a double silicon vacancy, V_{2Si} (Fig. 1(e)). A combined vacancy involving the simultaneous removal of one silicon and one carbon atom led to the formation of a dual vacancy labeled as V_{SiC}, as shown in Fig. 1(f).

Antisite defects were also examined in this study. Replacing a silicon atom with a carbon atom yielded the antisite defect C_{Si} (Fig. 1(g)), while substituting a carbon atom with a silicon atom formed the Si_C defect (Fig. 1(h)). The exchange of positions between neighboring silicon and carbon atoms resulted in a double antisite defect, designated as Si ↔ C, as depicted in Fig. 1(i).

We chose thirteen substitutional dopants because their atomic size is compatible with silicon, their electronegativity is different, and they have been shown to work in similar materials in experiments. These dopants include As, Bi, Ga, Ge, P, Pb, Sb, Sn, In, Te, Ca, K, and Mg, producing the respective configurations: As_{Si}, Bi_{Si}, Ga_{Si}, Ge_{Si}, P_{Si}, Pb_{Si}, Sb_{Si}, Sn_{Si}, In_{Si}, Te_{Si}, Ca_{Si}, K_{Si}, and Mg_{Si}, as illustrated in Fig. 2(a)–(m). Additionally, nitrogen and boron doping were achieved by replacing a carbon atom with one nitrogen or one boron atom, resulting in N_C (Fig. 2(n)) and B_C (Fig. 2(o)), respectively. Phosphorus, arsenic, and antimony are all group V elements. Gallium, indium, and boron are all group III elements. To broaden the chemical range and see how they affect localized electronic states and light emission, calcium, magnesium, potassium, tellurium, bismuth, lead, and tin were added. Researchers have added a lot of dopants to SiC, GaN, and ZnO using methods like ion implantation, molecular beam epitaxy, and chemical vapor deposition. Phosphorus and arsenic are known to provide shallow donor levels in 4H-SiC,[95,96] while gallium and indium have been used to make SiC and ZnO p-type conductors.[97,98] High-temperature growth and implantation have made it possible to dope magnesium and calcium.[99,100] Bismuth and tellurium have been used to change the optoelectronic properties of chalcogenide semiconductors and two-dimensional materials.[101,102] The types of defects and dopants used for this study are a good mix of what can be done with computers and what is useful in experiments. This choice gives us a strong basis for looking at how 2D-SiC can be changed for possible uses in solid-state lighting.

2.2 Device modelling

In this work, we propose a novel LED structure employing 2D SiC as an active layer under three different conditions: pristine, defect-engineered, and doped. The performance of this LED is strongly influenced by the band gap of the 2D SiC layer. Our proposed 2D SiC-based LED may be manufactured by integrating epitaxial growth,[103] a solid-state joining process,[104] with

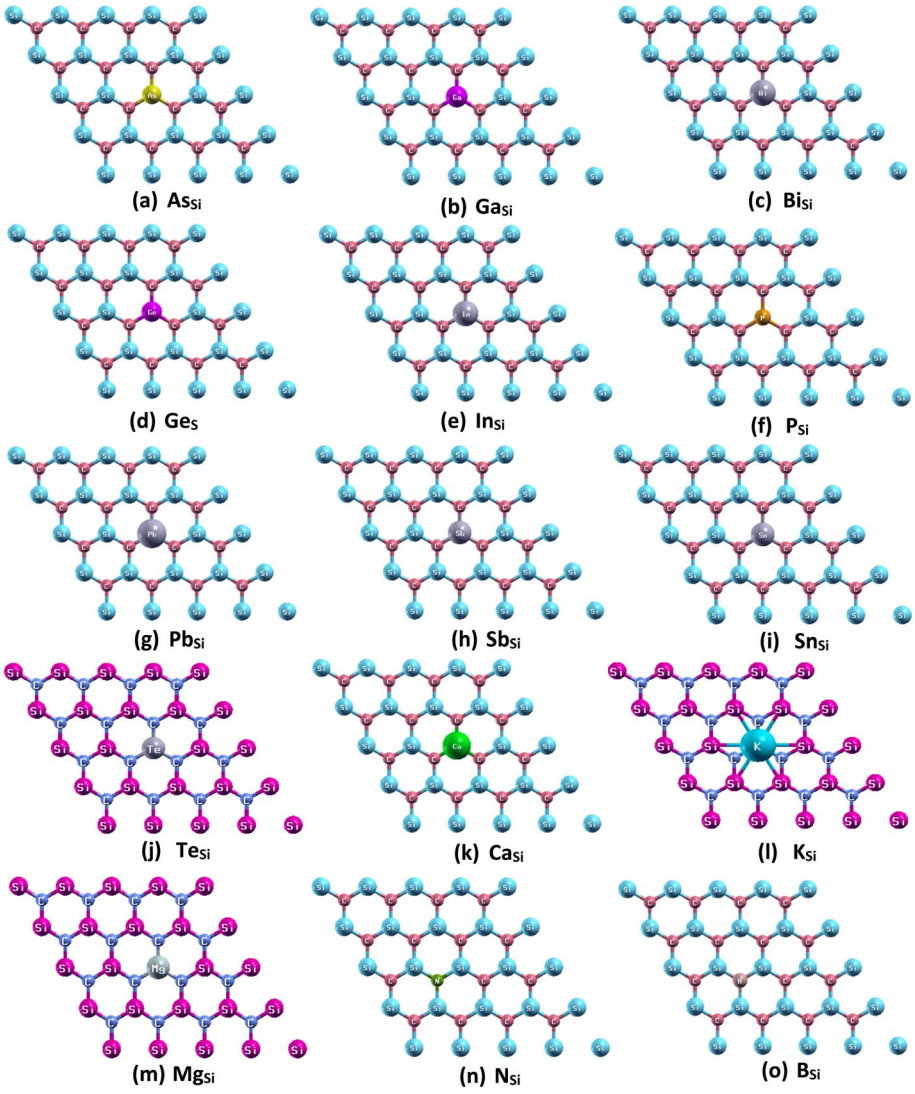

Fig. 2 The structural configuration of point doping in a monolayer of SiC: (a) As_{Si}, (b) Bi_{Si}, (c) Ga_{Si}, (d) Ge_{Si}, (e) In_{Si}, (f) P_{Si}, (g) Pb_{Si}, (h) Sb_{Si}, (i) Sn_{Si}, (j) Te_{Si}, (k) Ca_{Si}, (l) K_{Si}, (m) Mg_{Si}, (n) N_C, (o) B_C.

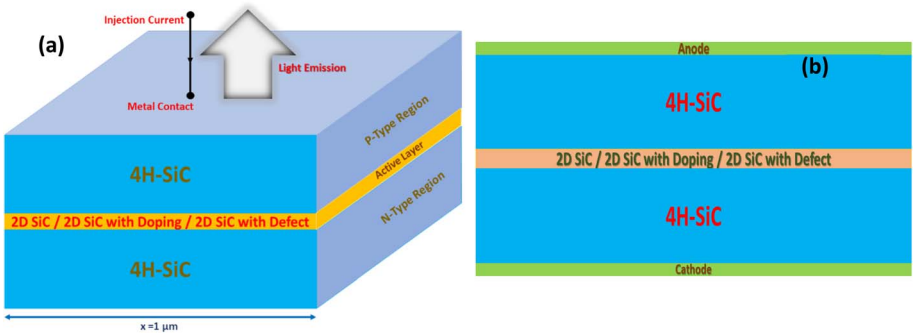

Fig. 3 A schematic of SiC-based light-emitting diode: (a) 3D view; (b) cross-section of the front view.

diffusion bonding,[105] a state-of-the-art methodology for constructing SiC devices.[106] Fig. 3 shows the basic schematic diagram of the proposed structure. To model the fabrication process, we considered the diffusion welding technique, which involves applying high temperature and pressure to bond thick wafers of different materials. As illustrated in Fig. 4, this method is used to join two dissimilar material wafers under elevated thermal and mechanical conditions. Following this concept, we performed microscale simulations of the proposed SiC-based single quantum well (SQW) LED structure using various 2D SiC active layers. These simulations were carried out using the SILVACO TCAD software suite.

In our simulated device, we have implemented the diffusion welding approach to directly link the N-type 4H-SiC thick wafer, rather than using epitaxial layers for deposition. Following this, a thin intrinsic layer of two-dimensional silicon carbide (2D SiC) in its pristine, doped, or defect-engineered form was deposited onto the N-type 4H-SiC substrate to form a layered structure. In the last stage, consisting of an N-type 4H-SiC and an intrinsic epilayer, was combined with a thick P-type 4H-SiC wafer using the same method as the diffusion bonding strategy. The simulated light-emitting diode has been constructed using heavily doped P-type and N-type 4H-SiC layers, with concentrations of 1 $\times$ 10^{18} cm^{-3} because it is a standard value used in high-performance SiC optoelectronic devices. The concentrations are in line with what is usually achieved using experimental methods like ion implantation or *in situ* doping during chemical vapor deposition (CVD).[107,108] After that, the dopants are activated by high-temperature annealing at temperatures above 1600 °C. Adding phosphorus and nitrogen to 4H-SiC has made it N-type doped, with carrier concentrations between 10^{17} and 10^{19} cm^{-3}, as shown in studies of implantation and diffusion.[95,96,109] Using hot-wall CVD techniques, it has been shown that P-type doping with aluminum can reach similar levels.[110,111] The concentration of doping has a big effect on how well a device works. Higher doping levels improve carrier injection and conductivity, which lowers series resistance. But this can also cause more free-carrier absorption, Auger recombination, and band tailing linked to dopants, all of which could make it harder to get light out. On the other hand, lower doping concentrations may help with light extraction, but they often make carrier injection and current density lower. The chosen concentration of 1 $\times$ 10^{18} cm^{-3} strikes a good balance between improving electrical qualities and making sure there is a lot of visual output.

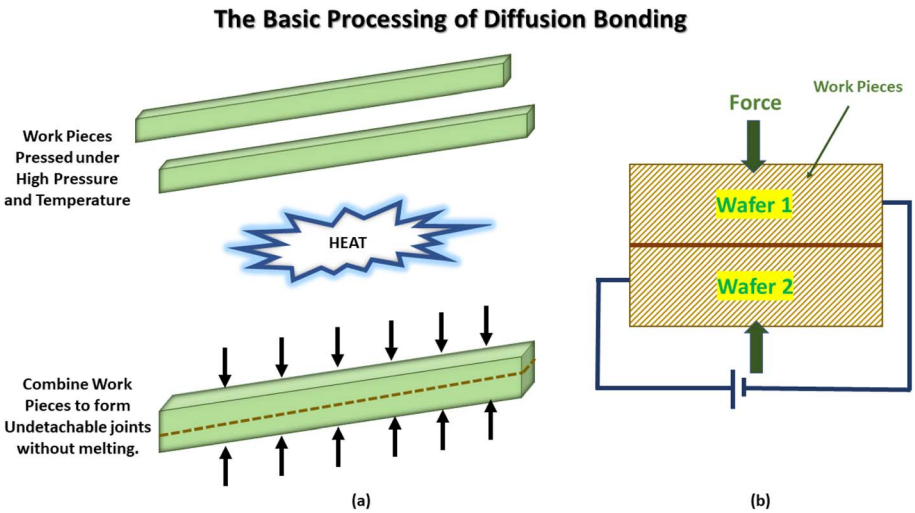

Fig. 4 Process diagram for diffusion welding (a) two wafers bonded together at high heat and pressure; (b) wafers 1 and 2 bonded directly together at high pressure.[105]

Table 1 Summary of electrical and optical properties of the layer, and device properties for various device configurations

	Electrical characteristics of layer						Optical property of layer		Device properties		
	Effective mass				Mobility ($cm^2 V^{-1} s^{-1}$)						
Device configuration	m_n^*	m_p^*	Band gap (eV)	Direct/indirect band gap	μ_n	μ_p	Real part of permittivity	Imaginary part of permittivity	λ_{mid} (nm)	Peak power spectral density ($W cm^{-1} eV^{-1}$)	LEE (%)
Pristine	2.54	1.78	2.57	Direct	277	198	7.65(λ_b) 5.46(λ_g) 5.29(λ_r)	3.57(λ_b) 0.33(λ_g) 0.13(λ_r)	476	4.87	10.27
V_C	—	—	1.13	Indirect	—	—	—	—	—	—	—
V_{Si}	—	—	2.21	Indirect	—	—	—	—	—	—	—
V_{2C}	—	—	0.95	Indirect	—	—	—	—	—	—	—
V_{2Si}	—	—	0.64	Indirect	—	—	—	—	—	—	—
V_{SiC}	—	—	0.95	Indirect	—	—	—	—	—	—	—
C_{Si}	2.44	1.66	1.99	Direct	288	212	—	—	612	3.59	—
Si_C	—		2.00	Indirect	—	—	—	—	—	—	—
Si ↔ C	2.13	2.87	1.41	Direct	330	122	—	—	855	2.28	—
As_{Si}	3.84	1.73	1.96	Direct	183	203	4.94(λ_b) 7.01(λ_g) 6.59(λ_r)	6.42(λ_b) 2.62(λ_g) 1.32(λ_r)	619	3.59	21.53
Bi_{Si}	—	—	2.00	Indirect	—	—	—	—	—	—	—
Ga_{Si}	3.14	2.0	2.50	Direct	224	176	4.92(λ_b) 3.44(λ_g) 1.45(λ_r)	2.78(λ_b) 0.46(λ_g) 0.42(λ_r)	490	4.74	17.55
Ge_{Si}	—	—	2.51	Indirect	—	—	—	—	—	—	—
In_{Si}	2.38	2.14	2.45	Direct	296	165	—	—	500	4.57	8.18
P_{Si}	3.14	1.76	2.01	Direct	224	200	6.39(λ_b) 6.85(λ_g) 6.44(λ_r)	0.77(λ_b) 2.42(λ_g) 6.82(λ_r)	606	3.68	12.66
Pb_{Si}	2.33	1.90	2.47	Direct	302	185	4.32(λ_b) 0.85(λ_g) 2.94(λ_r)	4.22(λ_b) 0.78(λ_g) 0.77(λ_r)	495	4.62	26.85
Sb_{Si}	—	—	2.01	Indirect	—	—	—	—	—	—	—
Sn_{Si}	2.71	1.85	2.50	Direct	259	190	—	—	490	4.73	11.29
Te_{Si}	6.28	1.69	1.38	Direct	112	208	—	—	871	2.38	10.41
Ca_{Si}	2.94	14.5	2.31	Direct	239	24	4.56(λ_b) 4.65(λ_g) 2.95(λ_r)	7.5(λ_b) 1.77(λ_g) 1.65(λ_r)	529	4.15	16.03
K_{Si}	2.22	15.98	1.85	Direct	316	22	4.79(λ_b) 7.47(λ_g) 4.38(λ_r)	8.13(λ_b) 1.76(λ_g) 0.96(λ_r)	660	3.15	22.57
Mg_{Si}	3.44	2.74	2.49	Direct	204	128	4.51(λ_b) 2.36(λ_g) 0.08(λ_r)	5.18(λ_b) 1.29(λ_g) 1.50(λ_r)	492	4.69	21.46
N_C	—	—	2.54	Indirect	—	—	—	—	—	—	—
B_C	2.87	2.59	2.13	Direct	245	135	7.01(λ_b) 4.65(λ_g) 3.24(λ_r)	4.21(λ_b) 1.62(λ_g) 0.72(λ_r)	570	3.93	20.48

In addition, we have taken into account the option of using a direct bonding procedure in our simulations, as this method may also be used for very thin layers of materials.[105] By combining epitaxial growth, a cutting-edge technology for fabricating SiC devices,[106] with diffusion bonding, a solid-state joining method,[104] we can potentially manufacture our proposed 2D SiC-based LED. The central focus of this study is to investigate the impact of the active layer composition whether pristine 2D SiC, defected 2D SiC, or doped 2D SiC on the device's performances. For establishing electrical connectivity, ideal materials were assumed for both the anode and cathode contacts, ensuring optimal charge injection and extraction. This assumption makes the study easier by only looking at carrier injection and recombination in the active region and not contact resistance. Charge injection can be affected by contact barriers and interface states. These factors will be included to future simulations to help us better understand how devices work.[109]

A variety of appropriate physical models relevant to LEDs were applied in the simulations. The POLARIZATION command within the MODEL statement of SILVACO TCAD was used to implement and activate the polarization model effectively. Carrier mobilities in the simulation were clearly shown for the bulk 4H-SiC and monolayer 2D-SiC areas. The Caughey–Thomas equation was used to simulate the mobility of P-type and N-type 4H-SiC layers, which depends on the amounts of doping.[112,113] The degradation of mobility in 4H-SiC layers due to doping was modeled using the Caughey–Thomas empirical relation, which is automatically activated upon enabling CONMOB. This approach is often used for SiC-based devices, and experiments show that it works. In the 2D-SiC active layer, constant values of electron and hole mobilities were utilized, based on the first-principles results obtained from our calculations. The values are displayed in Table 1.

In this study, we used advanced physical models from Silvaco Atlas to precisely represent how the LED structure behaves when light is present. The Fermi model could use Fermi–Dirac statistics for carrier distributions, which is more accurate than Boltzmann statistics, especially when there is a lot of doping or the temperature is low. The consrh model is used in SILVACO TCAD included Shockley–Read–Hall (SRH) recombination, which takes into consideration trap-assisted electron–hole recombination through defect states in the bandgap. To look at non-radiative recombination at high carrier densities, the auger model was turned on. This made it possible to model energy transfer from recombining carriers to a third carrier instead of photon emission. The optr model added optical recombination mechanisms, which made it possible to model radiative processes that are important for light emission in LEDs. Also, spontaneous emission was thought to be able to catch photon production from direct electron–hole recombination. We employed the Lorentz model to account for spectral broadening in the emitted light. We applied a Lorentzian line shape to make the device's emission spectrum look like it really is. These models worked together to make sure that the LED's transport, recombination, and emission phenomena were all fully and physically true.

3 Results

3.1 Electronic properties

Fig. 5(a) illustrates that the pristine 2D SiC possesses a direct bandgap, with the conduction band minimum (CBM) and valence band maximum (VBM) located at the *K* point. The calculated bandgap for the pristine structure is 2.57 eV, which aligns well with values reported in previous studies.[44] To investigate the impact of vacancy defects on the electronic structure, several defect configurations were considered, as shown in Fig. 5(b)–(f). The carbon vacancy (V_C) was introduced by removing a single carbon atom from the relaxed $4 \times 4 \times 1$ supercell. The resulting structure exhibits an indirect bandgap of 1.13 eV, with transitions occurring between the *M* and *K* points, as shown in Fig. 5(b). The silicon vacancy (V_{Si}) configuration, formed by removing one silicon atom, exhibits an indirect bandgap of 2.21 eV, with the CBM located at the *K* point and the VBM at the *Γ* point (Fig. 5(c)).

For divacancy configurations, the carbon divacancy (V_{2C}), obtained by removing two carbon atoms, shows an indirect bandgap of 0.9531 eV with the CBM at *Γ* and the VBM at *K* [Fig. 5(d)]. The silicon divacancy (V_{2Si}), formed by removing two silicon atoms, reveals a direct bandgap of 0.64 eV at the *Γ* point [Fig. 5(e)]. The silicon–carbon divacancy (V_{SiC}), formed by simultaneously removing one silicon and one carbon atom, exhibits an indirect bandgap of 0.95 eV, with the CBM at *Γ* and the VBM at *K* [Fig. 5(f)].

Antisite defects were also explored by substituting a silicon atom with a carbon atom (C_{Si}), a carbon atom with a silicon atom (Si_C), and by interchanging the positions of a silicon and a carbon atom (Si ↔ C). The corresponding electronic band structures are depicted in Fig. 5(g)–(i). The C_{Si} and Si ↔ C configurations both show direct bandgaps at the *K* point, with calculated values of 1.99 eV and 1.41 eV, respectively. In contrast, the Si_C structure presents an indirect bandgap of 2.00 eV, with the CBM at *Γ* and the VBM at *K*.

The effects of substitutional doping at the silicon site were examined using elements such as As, Bi, Ga, Ge, In, P, Pb, Sb, Sn, Te, Ca, K, and Mg. Fig. 6(a)–(m) show the band structures of these doped configurations. Dopants including As, Ga, In, Pb, Sn, Ca, K, and Mg yield direct bandgaps at the *K* point. The respective bandgap values are 1.96 eV (As_{Si}), 2.50 eV (Ga_{Si}), 2.47 eV (In_{Si}), 2.50 eV (Pb_{Si}), 1.38 eV (Sn_{Si}), 1.84 eV (Ca_{Si}), 2.48 eV (K_{Si}), and 2.31 eV (Mg_{Si}). In contrast, Bi, Ge, and Sb dopants result in indirect bandgaps, where the CBM is located at *Γ* and the VBM at *K*. The corresponding bandgaps are 2.00 eV (Bi_{Si}), 2.51 eV (Ge_{Si}), and 2.01 eV (Sb_{Si}), as shown in Fig. 6(b), (d) and (h), respectively.

Doping at the carbon site with nitrogen (N_C) and boron (B_C) were also analyzed. The N_C structure shows an indirect bandgap of 2.54 eV with the CBM at *Γ* and the VBM at *K* (Fig. 6(n)), whereas the B_C configuration yields a direct bandgap of 2.14 eV at the *K* point (Fig. 6(o)).

The effective mass of charge carriers is a key parameter in semiconductors, as it directly influences the carrier mobility and, consequently, affects the photoelectric and thermoelectric

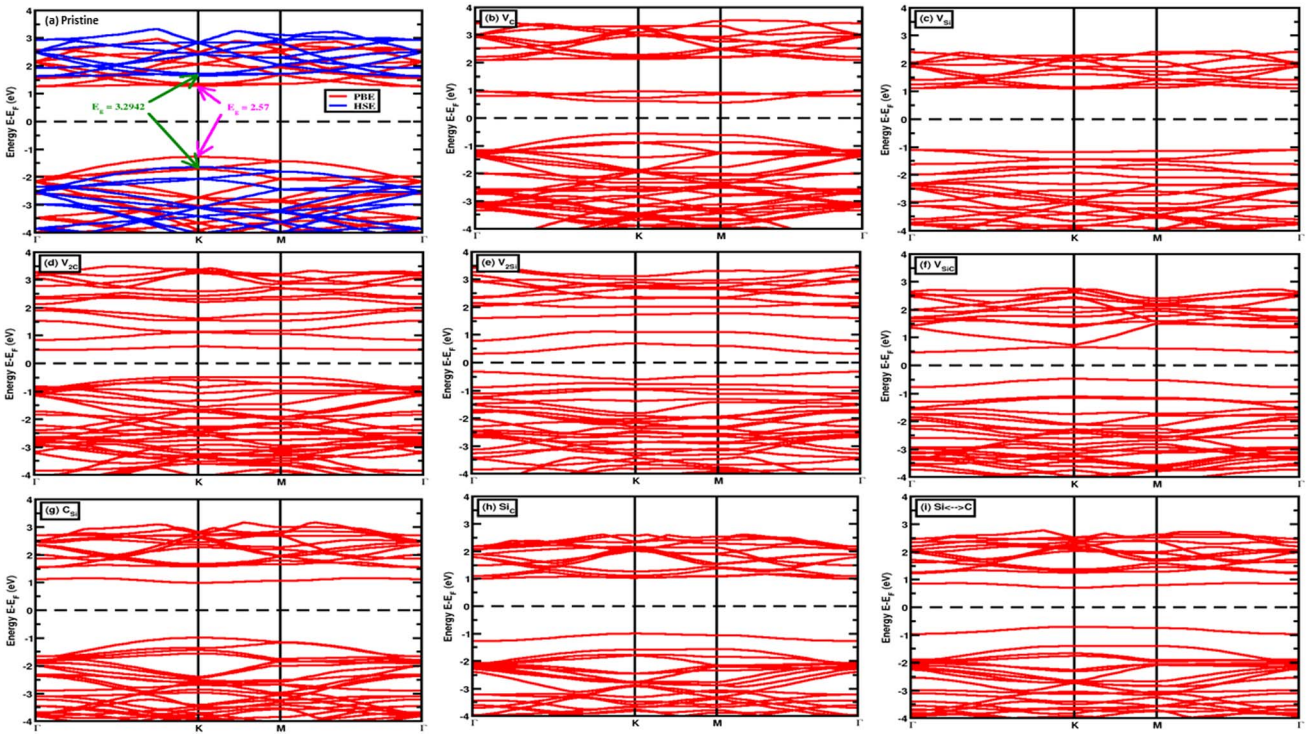

Fig. 5 (a) The electrical band diagrams of a pristine 2D-SiC monolayer; the electrical band diagrams of single vacancy defect in a monolayer of SiC: (b) V_C, (c) V_{Si}; the electrical band diagrams of double vacancy defect in a monolayer of SiC: (d) V_{2C}, (e) V_{2Si}, (f) V_{SiC}; the electrical band diagrams of antisite defect in a monolayer of SiC: (g) C_{Si}, (h) Si_C, (i) Si ↔ C.

performance of the material.[114] In this section, we report the calculated effective masses of electrons and holes for pristine and defect-engineered 2D-SiC, for which, to the best of our knowledge, no prior comprehensive data exist.

The effective masses of holes and electrons were estimated by performing second-order parabolic fitting of curves at the conduction band minimum and the valence band maximum, respectively. Effective masses of carriers:

$$\frac{1}{m^*} = \frac{1}{h^2}\frac{\partial^2 E(k)}{\partial k^2}$$

where m^* denotes the effective mass, h is the Planck constant, $E(k)$ is the energy as a function of wave vector k. The effective masses are normalized with respect to the free electron mass m_0.

For the pristine SiC monolayer, the effective electron and hole masses at the band extrema were computed to be $m_n^* = 2.54m_0$ (at the K point) and $m_p^* = 1.78m_0$ (at the K point), respectively. Low effective masses correspond to high carrier mobility, making such defect structures promising candidates for photovoltaic applications due to their potential for efficient charge transport.[47,115] On the other hand, higher effective masses result in lower carrier mobility, which can be advantageous for thermoelectric applications, where reduced mobility contributes to more effective conversion of waste heat into electrical energy.[116,117]

Subsequently, we determined the electron mobility and hole mobility of SiC in the various conditions by the following equations:

$$\mu = \frac{e\tau}{m^*}$$

The relaxation period τ for semiconductor solids generally ranges from 10^{-13} to 10^{-14}.[112,118–121] In this work, the mobility computation has utilized a value of τ of 10^{-13}.

To investigate the impact of structural defects on charge carrier transport, we extended our calculations to various defect and doping configurations. The effective masses and carrier mobility were calculated for both defective and doped 2D-SiC systems, specifically focusing on those configurations that exhibit a direct band gap. The extracted values are summarized in Table 1.

3.2 Optical properties

This section presents a detailed examination of the optical characteristics of pristine 2D SiC and its variations incorporating point defects and dopants. The examination highlights essential parameters relevant to optoelectronic applications, such as the real and imaginary parts of the dielectric constant, refractive index, absorption coefficient, and electron energy loss function.

The absorption spectra don't include excitonic corrections, which are known to affect how two-dimensional materials respond optically. Even though this is a problem, we still want to compare how different defect and dopant systems affect optical behavior. The predicted optical gap for pure 2D-SiC is about 2.6 eV, which is in line with experimental photoluminescence measurements. This shows that PBE is enough

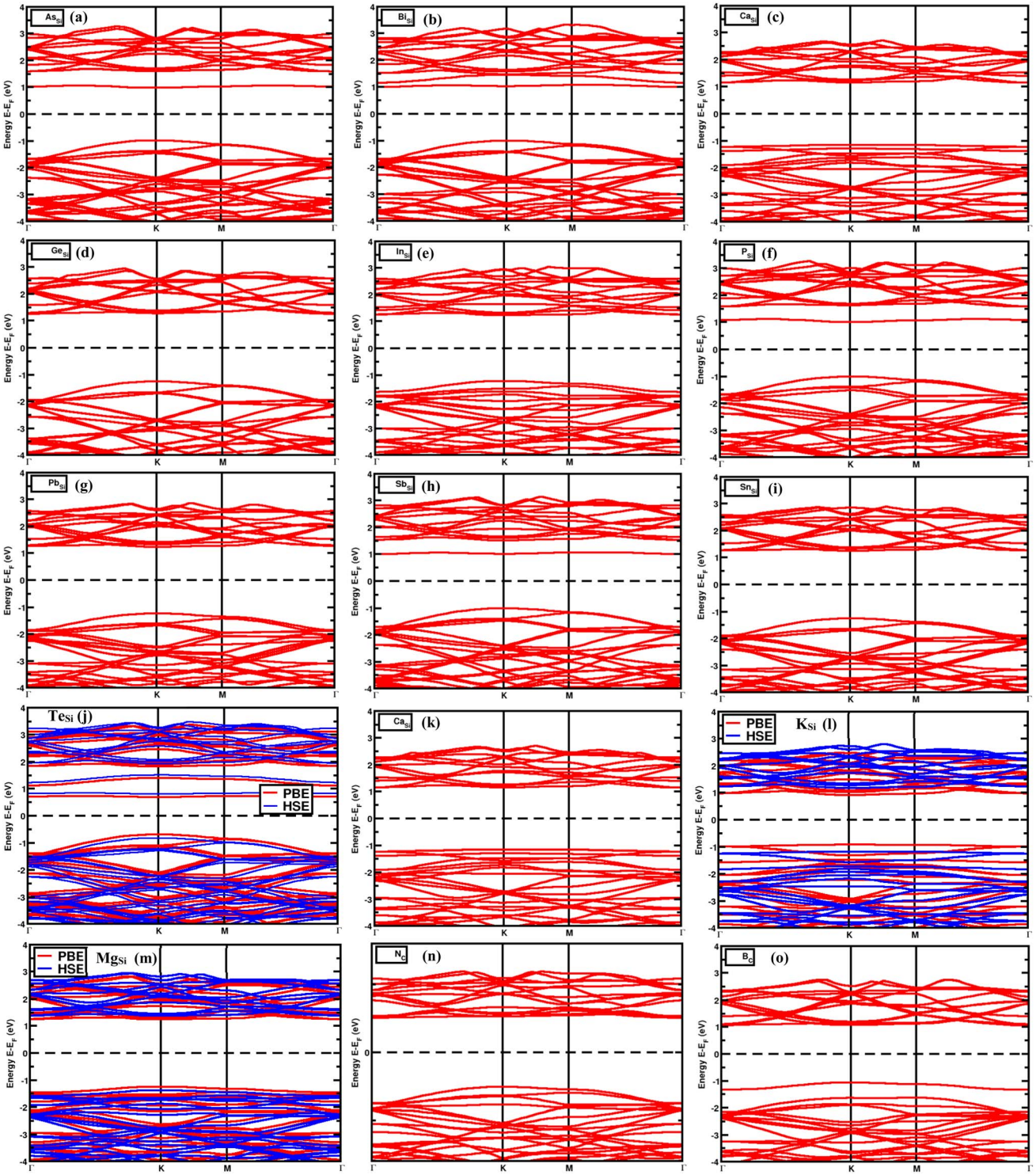

Fig. 6 The electrical band diagrams of point doping in a monolayer of SiC: (a) As_{Si}, (b) Bi_{Si}, (c) Ga_{Si}, (d) Ge_{Si}, (e) In_{Si}, (f) P_{Si}, (g) Pb_{Si}, (h) Sb_{Si}, (i) Sn_{Si}, (j) Te_{Si}, (k) Ca_{Si}, (l) K_{Si}, (m) Mg_{Si}, (n) N_C, (o) B_C.

for looking at qualitative trends. The good agreement is probably due to the fact that the computed spectra don't include exciton binding energy and the bandgap underestimate was canceled.

The complex dielectric function is defined as $\varepsilon(\omega) = \varepsilon_1(\omega) + i\varepsilon_2(\omega)$, where $\varepsilon_1(\omega)$ represents the real part, and $\varepsilon_2(\omega)$ denotes the imaginary part.[122,123] The behavior of the real part of the dielectric function, $\varepsilon_1(\omega)$, offers critical insights into how light interacts with SiC, particularly in terms of its propagation

characteristics and electronic polarizability. The real part of the dielectric function, $\varepsilon_1(\omega)$ reflects how the material responds to incident electromagnetic waves, governing both dispersion and energy storage in the system. The low-frequency or long wavelengths limit of $\varepsilon_1(\omega)$ as ω approaches 0 indicates a relatively high static dielectric constant of about 3.9, suggesting significant polarization effects in the in-plane direction of the pristine SiC, as shown in Fig. 7(a). This high value suggests robust dielectric screening and pronounced responsiveness to external fields. Across the visible spectrum, from roughly 850 nm down to 480 nm, $\varepsilon_1(\omega)$ displays a gradual increase in magnitude, peaking near 410 nm. This trend implies enhanced optical activity and a resonant interaction with photons in this range. A decrease in $\varepsilon_1(\omega)$ is observed with a further reduction in wavelength, indicating enhanced light–matter interaction and a possible increase in optical absorption processes. This parameter turned negative in the ultraviolet (UV) region, implying a potential for plasmonic behavior in that region. Moreover, the presence of distinct peaks in $\varepsilon_1(\omega)$ corresponds to allowed interband transitions, likely originating from energy states near Van Hove singularities in the electronic band structure.[123] These optical transitions highlight the intrinsic anisotropy and dipole-allowed excitations within the material. Taken together, the high static dielectric response, strong visible-range activity, and spectral features of $\varepsilon_1(\omega)$ affirm that SiC is a promising platform for optoelectronic applications, particularly those operating in the infrared and visible regimes.

In the case of single vacancy defects, the carbon vacancy (V_C) configuration demonstrates a relatively high $\varepsilon_1(\omega)$ value at low frequencies, indicating enhanced dielectric screening and elevated electronic polarizability, as illustrated in Fig. 7(b). Conversely, the silicon vacancy (V_{Si}) configuration exhibits a negative $\varepsilon_1(\omega)$ value, suggestive of metallic or plasmonic behavior, as depicted in Fig. 7(b).

Double vacancy structures, including V_{2C}, V_{2Si}, and V_{SiC}, exhibit elevated $\varepsilon_1(\omega)$ values in the low-frequency regime, as illustrated in Fig. 7(d)–(f), reflecting pronounced static polarizability and effective dielectric screening at long wavelengths. As the excitation wavelength decreases, $\varepsilon_1(\omega)$ transitions to negative values, indicating the onset of plasmonic behavior and a metallic-like optical response at higher photon energies. The transition from robust dielectric properties in the infrared and visible spectra to negative permittivity in the ultraviolet spectrum highlights the promise of these defect-engineered 2D-SiC for adjustable optoelectronic and plasmonic uses.

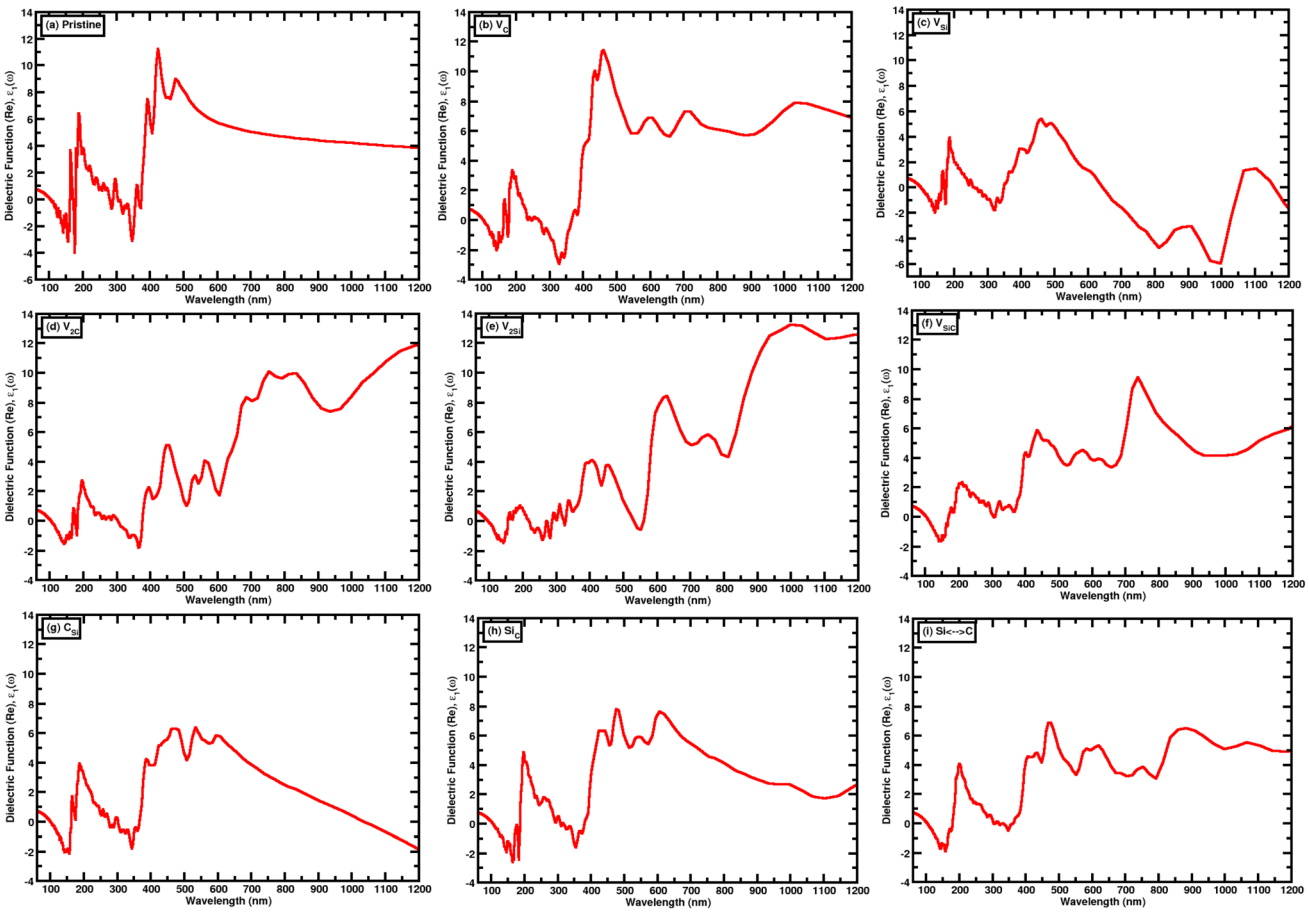

Fig. 7 (a) The real part of the dielectric spectrum of a pristine 2D-SiC monolayer; the real part of the dielectric spectrum of single vacancy defect in a monolayer of SiC: (b) V_C, (c) V_{Si}; the real part of the dielectric spectrum of double vacancy defect in a monolayer of SiC: (d) V_{2C}, (e) V_{2Si}, (f) V_{SiC}; the real part of the dielectric spectrum of antisite defect in a monolayer of SiC: (g) C_{Si}, (h) Si_C, (i) Si ↔ C.

Antisite defects exhibit distinct dielectric behavior depending on the atomic configuration. The C_{Si} defect shows a negative $\varepsilon_1(\omega)$ value at very long wavelengths, indicating a metallic or plasmonic optical response, as shown in Fig. 7(g). In contrast, the Si_C and Si ↔ C configurations demonstrate high $\varepsilon_1(\omega)$ values in the same spectral range, suggesting enhanced static dielectric screening and elevated in-plane polarizability, as presented in Fig. 7(h) and (i), respectively.

Doping significantly alters the dielectric response of 2D-SiC. In particular, dopant configurations such as As_{Si} (Fig. 8(a)), Bi_{Si} (Fig. 8(b)), Ge_{Si} (Fig. 8(d)), P_{Si} (Fig. 8(f)), Sb_{Si} (Fig. 8(h)), Sn_{Si} (Fig. 8(i)), Te_{Si} (Fig. 8(j)), and N_C (Fig. 8(n)) exhibit notably high values of the real part of the dielectric function, $\varepsilon_1(\omega)$, in the low-frequency or long-wavelength regime. This behavior indicates strong static polarizability and efficient dielectric screening, underscoring the doped structures' responsiveness to external electric fields in this spectral region. At higher energies, particularly within the ultraviolet range, $\varepsilon_1(\omega)$ transitions to negative values. This shift suggests the onset of plasmonic activity and a metallic-like optical response. The observed transition from a high positive dielectric constant at low energies to negative values at higher excitation energies reveals the potential of these doped SiC systems for tunable optoelectronic and plasmonic applications.

In contrast, doped configurations such as Ga_{Si} (Fig. 8(c)), In_{Si} (Fig. 8(e)), Pb_{Si} (Fig. 8(g)), Ca_{Si} (Fig. 8(k)), K_{Si} (Fig. 8(l)), Mg_{Si} (Fig. 8(m)), and B_C (Fig. 8(o)) exhibit negative values of the real part of the dielectric function, $\varepsilon_1(\omega)$, in the long-wavelength or low-frequency region. This behavior suggests a response similar to metallic or plasmonic characteristics, potentially arising from oscillations of free carriers or low-energy collective excitations. Furthermore, Ga_{Si}, In_{Si}, Pb_{Si}, and Ca_{Si} configurations display positive $\varepsilon_1(\omega)$ values within the shorter visible wavelength range, while K_{Si}, Mg_{Si}, and B_C show sustained positive values across a broader region of the visible spectrum. The continued presence of positive permittivity in the visible range further confirms the semiconducting nature of these materials, strengthening their applicability in optoelectronic and photonic devices.

The imaginary part of the dielectric function, $\varepsilon_2(\omega)$, is closely associated with the optical absorption characteristics of a material. It indicates the extent to which light is absorbed when it interacts with the material. As such, $\varepsilon_2(\omega)$ provides valuable insight into the electronic bandgap, which is linked to the energy of interband transitions occurring near the Fermi level. These transitions significantly influence the absorption properties of the material. Fig. 9(a) presents the variation of $\varepsilon_2(\omega)$ for pristine SiC. As shown in the graph, several prominent peaks appear near the energies corresponding to band transitions. Notably, the main absorption peak for pristine SiC occurs at a wavelength of around 380 nm. There has some prominent peak in UV region. This peak corresponds to strong interband transitions near the high-symmetry points of the Brillouin zone and reflects a high joint density of states.

For single vacancy defects, the carbon vacancy (V_C) configuration exhibits a relatively low value of the imaginary part of the dielectric function, $\varepsilon_2(\omega)$, in the high wavelength range, indicating minimal optical absorption in the infrared and near-visible regions, as shown in Fig. 9(b). In contrast, the silicon vacancy (V_{Si}) configuration demonstrates a significantly higher $\varepsilon_2(\omega)$ response within the same spectral range, as shown in Fig. 9(c). The significant absorption observed at low photon energies indicates strong optical transitions close to the band edge, probably due to notable excitonic.

Double vacancy structures, including V_{2C}, V_{2Si}, and V_{SiC}, exhibit non-zero value of the imaginary part of the dielectric function, $\varepsilon_2(\omega)$, in the high wavelength region, as shown in Fig. 9(d)–(f), respectively. This behavior indicates increased optical activity at photon energies below the bandgap of the pristine material, which is likely due to the presence of localized defect states within the bandgap. These configurations also display notable absorption peaks in the ultraviolet and visible regions, reflecting strong defect-related optical transitions. The observation of these peaks indicates that double vacancies create optically active defect states in the bandgap, potentially enabling radiative recombination processes. Similarly, antisite defect configurations such as C_{Si}, Si_C, and the Si ↔ C exchange defect also show a non-zero $\varepsilon_2(\omega)$ response in the high-wavelength region, further indicating sub-bandgap optical activity, as shown in Fig. 9(g) and (h). While all three defects exhibit pronounced absorption features in the ultraviolet region, the Si ↔ C configuration additionally shows significant absorption peaks in the visible range. The results indicate that double vacancies and antisite defects play a crucial role in affecting the optical characteristics of 2D-SiC, offering potential for the regulating of its optoelectronic properties for specific applications.

Doped SiC structures such as Ge_{Si}, Sn_{Si}, Te_{Si}, and N_C exhibit an imaginary part of the dielectric function, $\varepsilon_2(\omega)$, that remains close to zero, as shown in Fig. 10(d), (i), (j) and (n), respectively. This behavior reflects the wide bandgap nature of the material and the absence of low-energy electronic transitions. In contrast, dopants such as As_{Si} (Fig. 10(a)), Bi_{Si} (Fig. 10(b)), Ga_{Si} (Fig. 10(c)), In_{Si} (Fig. 10(e)), P_{Si} (Fig. 10(f)), Pb_{Si} (Fig. 10(g)), Sb_{Si} (Fig. 10(h)), Ca_{Si} (Fig. 10(k)), K_{Si} (Fig. 10(l)), Mg_{Si} (Fig. 10(m)), and B_C (Fig. 10(o)) result in a pronounced increase in $\varepsilon_2(\omega)$, indicating the formation of additional electronic states within or near the bandgap. These states promote optical transitions at sub-bandgap energies, leading to enhanced absorption in the low-photon-energy region. A significant rise in $\varepsilon_2(\omega)$ is observed at shorter wavelengths, with a strong absorption peak evident in the ultraviolet region for all doped configurations. This peak is attributed to interband transitions occurring near high-symmetry points in the Brillouin zone.

The refractive index serves as an essential optical parameter, detailing the propagation of light through a material and shaping its interaction with electromagnetic radiation. The refractive index of 2D-SiC is indicating of its intrinsic electronic structure and the robust in-plane bonding that exists between silicon and carbon atoms. The refractive index of 2D-SiC in its pristine, defect, and doped form is notably high within the visible spectrum, as illustrated in Fig. 11 and 12, varying with photon energy and polarization direction. The increased refractive index suggests a significant electronic polarizability

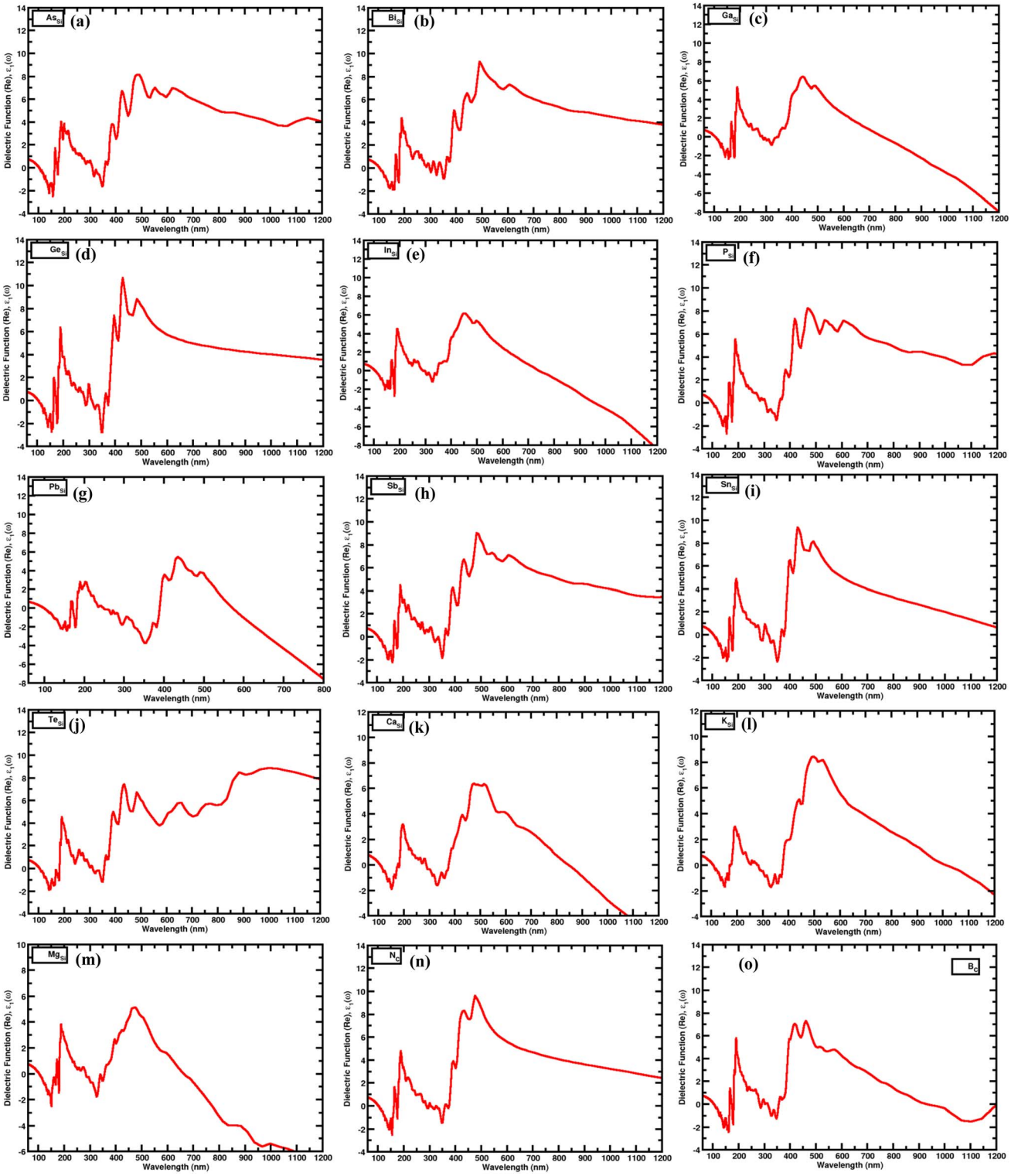

Fig. 8 The real part of the dielectric spectrum of point doping in a monolayer of SiC: (a) As_{Si}, (b) Bi_{Si}, (c) Ga_{Si}, (d) Ge_{Si}, (e) In_{Si}, (f) P_{Si}, (g) Pb_{Si}, (h) Sb_{Si}, (i) Sn_{Si}, (j) Te_{Si}, (k) Ca_{Si}, (l) K_{Si}, (m) Mg_{Si}, (n) N_C, (o) B_C.

and is closely associated with its moderate direct band gap and strong optical absorption across the ultraviolet to visible spectrum. The optical response of 2D-SiC exhibits increased tunability, attributed to its reduced dimensionality and interactions that are dominated by the surface. We can see that in Fig. 11 and 12, the refractive index is influenced by structural modifications such as defects and single atom doping, presenting opportunities to tailor its optical characteristics for

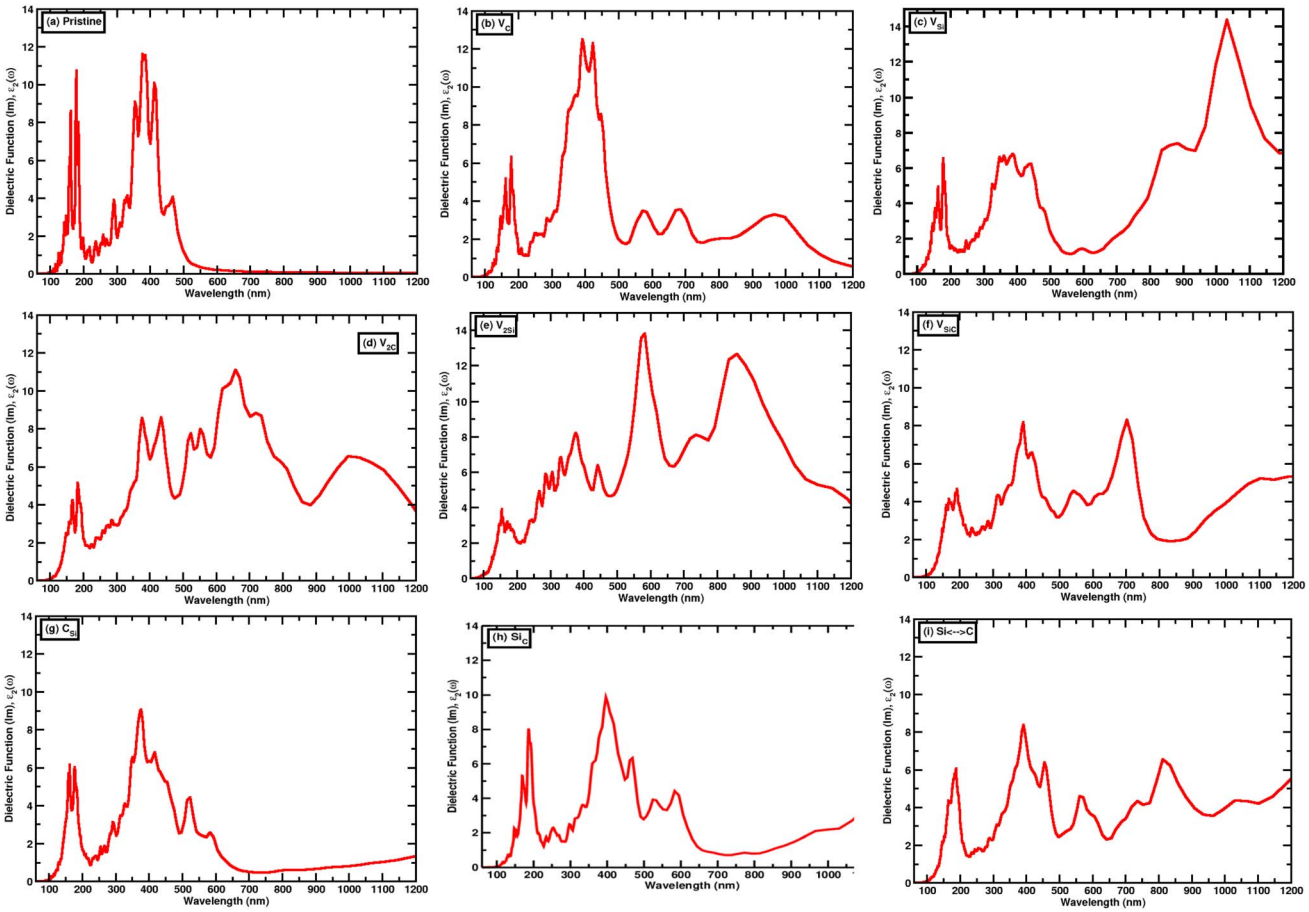

Fig. 9 (a) The imaginary part of the dielectric spectrum of a pristine 2D-SiC monolayer; the imaginary part of the dielectric spectrum of single vacancy defect in a monolayer of SiC: (b) V_C, (c) V_{Si}; the imaginary part of the dielectric spectrum of double vacancy defect in a monolayer of SiC: (d) V_{2C}, (e) V_{2Si}, (f) V_{SiC}; the imaginary part of the dielectric spectrum of antisite defect in a monolayer of SiC: (g) C_{Si}, (h) Si_C, (i) Si ↔ C.

specific applications. These properties make 2D-SiC a promising candidate for integration in nanoscale photonic and optoelectronic devices, including light-emitting diodes.

The absorption coefficient of pristine 2D-SiC, as shown in Fig. 13(a), becomes non-zero at the onset of the wavelength range, indicating the beginning of optical absorption from the visible region. This behavior corresponds to the material's bandgap of approximately 2.57 eV. The position and intensity of the absorption peaks are influenced by both the electronic band structure and lattice vibrations. The absorption edge is primarily determined by the bandgap energy, while the peak positions are also affected by excitonic interactions. A notable absorption maximum occurs near 180 nm.

Symmetry within the crystal structure plays a critical role in governing the selection rules for optical transitions. Materials with higher symmetry often restrict allowed transitions, resulting in fewer or weaker absorption features. Conversely, lower-symmetry structures can relax these selection rules, enabling stronger or more numerous optical transitions. In the case of 2D-SiC, the reduced symmetry permits enhanced optical transitions, which manifest as several strong absorption peaks in both the ultraviolet and visible regions. Furthermore, strong excitonic effects in 2D-SiC contribute to the appearance and shifting of these prominent absorption features.

The optical absorption spectra shown in Fig. 13 and 14 clearly reveal that defective SiC monolayers exhibit redshifted absorption onsets relative to the pristine monolayer. This redshift in absorption is primarily attributed to defect-induced states within the bandgap, which effectively narrow the optical gap. In the cases of vacancy type defects as shown Fig. 13(b)–(f), absorption starting from higher wavelengths (0 eV), resulting in metallic-like behavior. On the other hand, antisite type defects (Fig. 13(g) and (h)) where defect states are situated close to the CBM or VBM, the absorption spectra remain largely similar to the pristine monolayer with the first absorption peaks appearing in the visible range.

For doped SiC systems such as As_{Si} (Fig. 14(a)), Bi_{Si} (Fig. 14(b)), Ge_{Si} (Fig. 14(d)), P_{Si} (Fig. 14(f)), Pb_{Si} (Fig. 14(g)), Sb_{Si} (Fig. 14(h)), and Sn_{Si} (Fig. 14(i)) the absorption spectra remain largely similar to the pristine monolayer and their initial absorption peaks also lie in the visible region. In contrast, the doped SiC structures such as Ga_{Si} (Fig. 14(c)), In_{Si} (Fig. 14(e)), Te_{Si} (Fig. 14(j)), Ca_{Si} (Fig. 14(k)), K_{Si} (Fig. 14(l)), Mg_{Si} (Fig. 14(m)), N_C (Fig. 14(n)) and B_C (Fig. 14(o)) absorption starting from higher wavelengths (0 eV), resulting in metallic-like behavior.

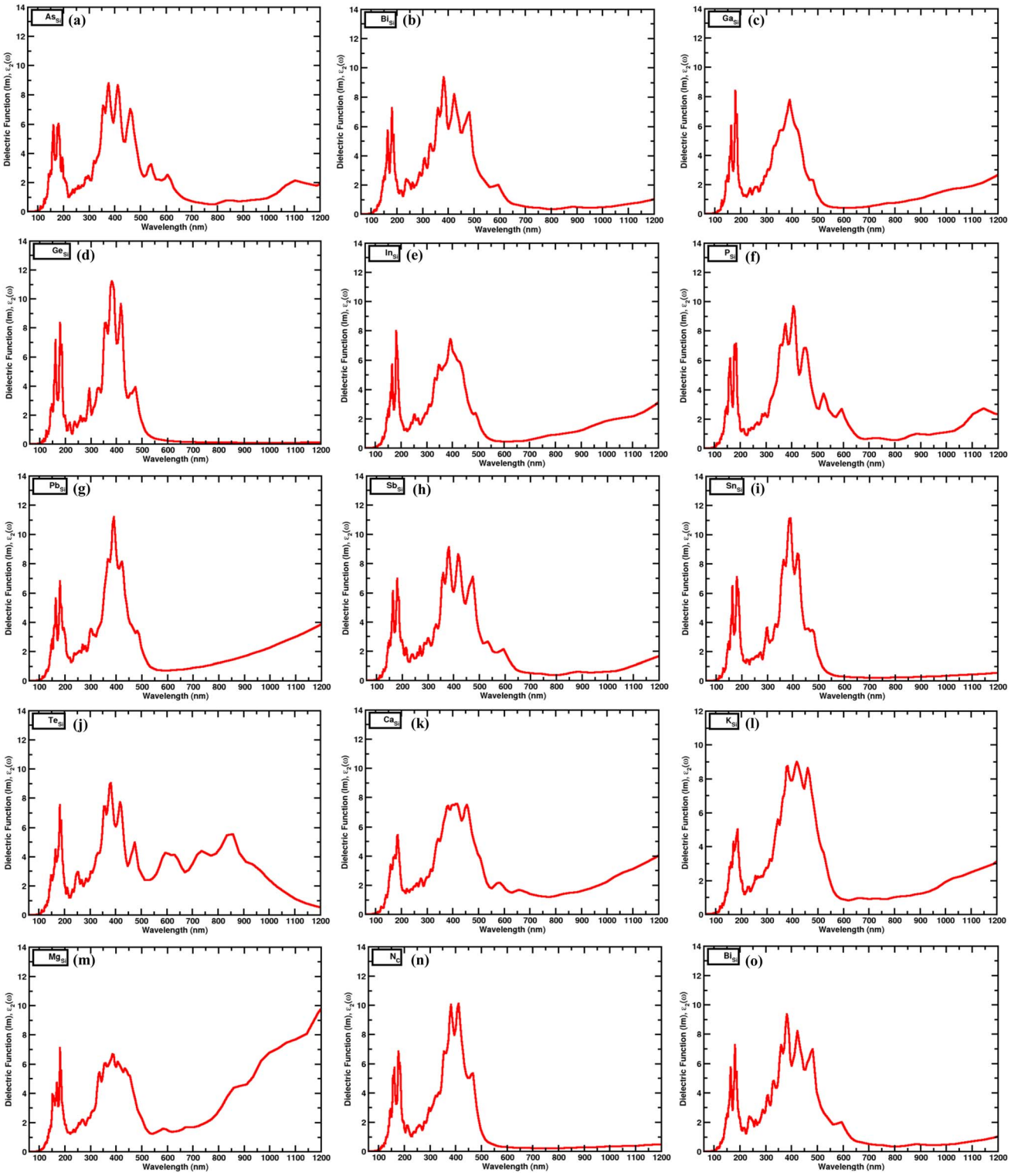

Fig. 10 The imaginary part of the dielectric spectrum of point doping in a monolayer of SiC: (a) As_{Si}, (b) Bi_{Si}, (c) Ga_{Si}, (d) Ge_{Si}, (e) In_{Si}, (f) P_{Si}, (g) Pb_{Si}, (h) Sb_{Si}, (i) Sn_{Si}, (j) Te_{Si}, (k) Ca_{Si}, (l) K_{Si}, (m) Mg_{Si}, (n) N_C, (o) B_C.

These structures also exhibit strong absorption peaks within the visible spectrum.

The observed strong absorption in the visible region highlights the potential of these defective and doped SiC structures for applications in solar-driven photocatalysis and visible-light LEDs. Additionally, the presence of absorption peaks in the IR region indicates suitability for IR LEDs, with potential uses in communication, sensing, and remote-control devices. The wide

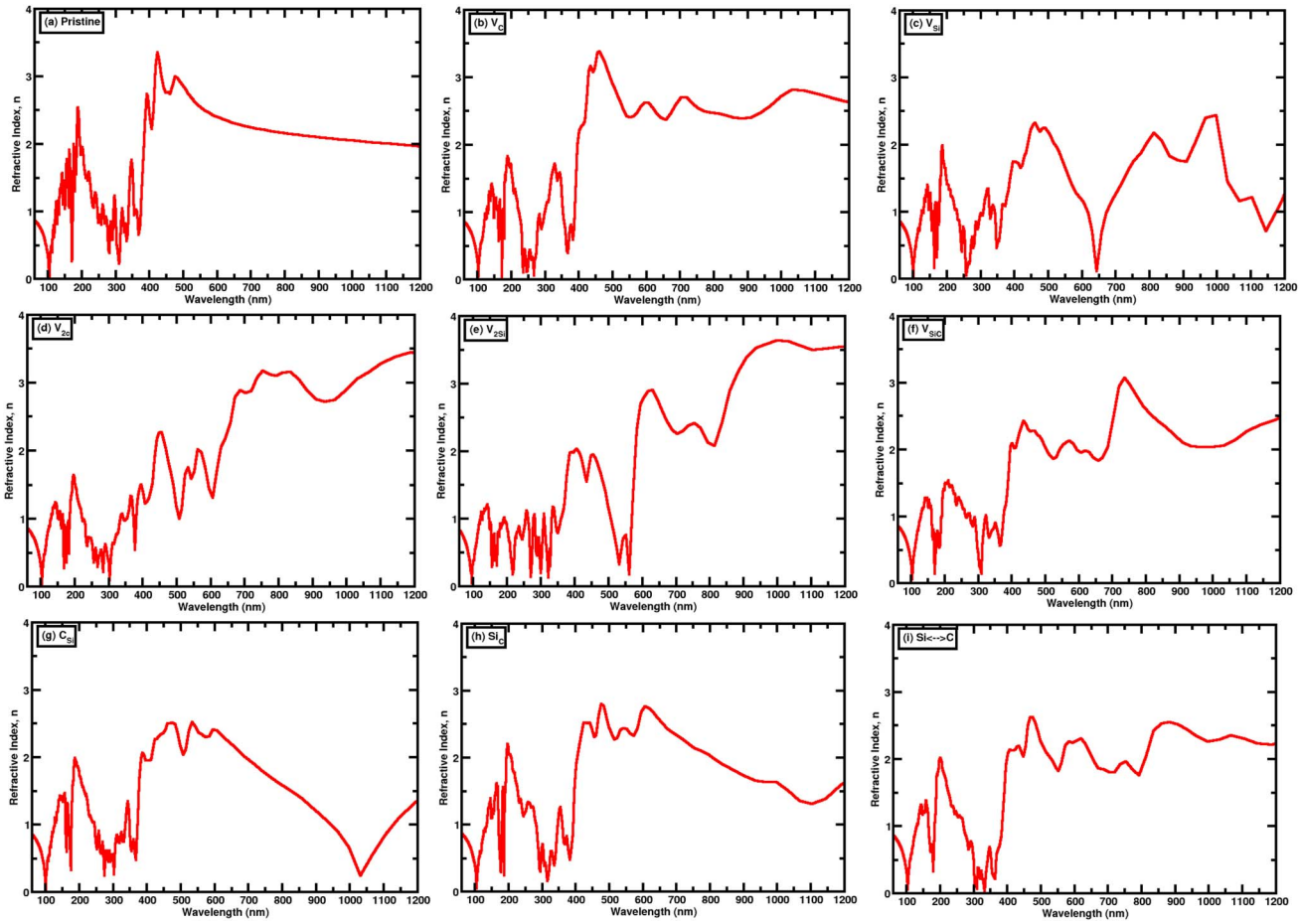

Fig. 11 (a) The refractive index of pristine monolayer SiC; the refractive index of single vacancy defect in a monolayer of SiC: (b) V_C, (c) V_{Si}; the refractive index of double vacancy defect in a monolayer of SiC: (d) V_{2C}, (e) V_{2Si}, (f) V_{SiC}; the refractive index of antisite defect in a monolayer of SiC: (g) C_{Si}, (h) Si_C, (i) Si ↔ C.

absorption coverage spanning UV, visible, and IR regions further highlights the applicability of these materials in diverse optoelectronic technologies.

The electron loss function (ELF) represents the amount of energy lost by electrons as they pass through a dielectric material. It provides critical information about the material's electronic structure, especially regarding energy dissipation and collective excitations such as plasmons. The peak positions and their intensities in the ELF spectrum reflect various electronic transitions and are closely related to the bandgap of the material. The ELF can be derived from the dielectric function using the standard relation involving the real and imaginary parts of the dielectric constant.

Fig. 15(a) presents the ELF for pristine 2D SiC. A strong peak appears near 105 nm, indicating a significant energy loss due to plasmon resonance. This feature is linked to the dielectric constant of the material and reveals its response to external electric and optical fields. Several prominent peaks are also observed in the ultraviolet (UV) region, for types of 2D SiC structure as shown in Fig. 15 and 16, suggesting that major plasmon excitations and energy losses occur in this range.

In the visible spectrum, the ELF displays moderate peaks, which correspond to interband electronic transitions. These transitions provide insight into the band structure and optical gap of 2D SiC. In the infrared region, the ELF decreases, showing that the material becomes more transparent and exhibits less energy loss in the infrared region.

Additionally, the presence of smaller energy peaks in the ELF may be attributed to phonon interactions and lower-energy excitations, hinting at underlying electron-phonon coupling mechanisms. Understanding these features is essential for exploring the electrical and optical characteristics of 2D-SiC, which has promising potential for applications in optoelectronics, high-power devices, and nanoelectronic systems.

3.3 Device performance

Now, we analyzed the various characteristics of our proposed LED device. Throughout this analysis, 2D SiC was utilized as an active layer under different conditions, including pure, defect, and doped states. We have already analyzed the electrical and optical characteristics of pure SiC, defected SiC, and doped SiC. Table 1 provides a comprehensive overview of the electrical properties, optical characteristics, and device performance for

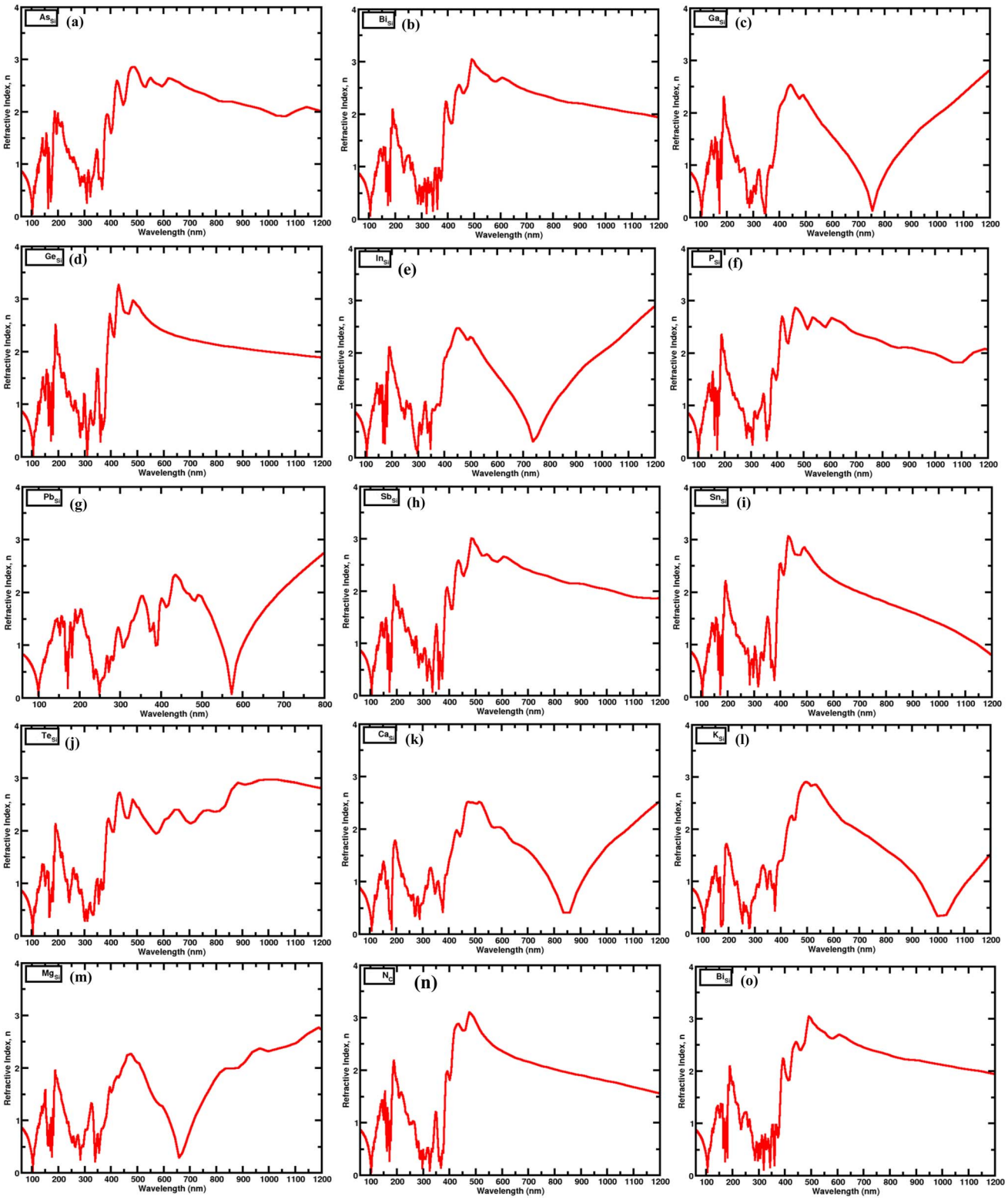

Fig. 12 The refractive index of point doping in a monolayer of SiC: (a) As_{Si}, (b) Bi_{Si}, (c) Ga_{Si}, (d) Ge_{Si}, (e) In_{Si}, (f) P_{Si}, (g) Pb_{Si}, (h) Sb_{Si}, (i) Sn_{Si}, (j) Te_{Si}, (k) Ca_{Si}, (l) K_{Si}, (m) Mg_{Si}, (n) N_C, (o) B_C.

various active layers. In this context, blue light (λ_b) is designated as 450 nm, green light (λ_g) as 550 nm, and red light (λ_r) as 650 nm.[124] Since LED technology is optimized for materials with a direct band gap, we focused on those materials exclusively. Afterward, we changed the active layer of our proposed LED by using defected SiC, and doped SiC. In order to create a white

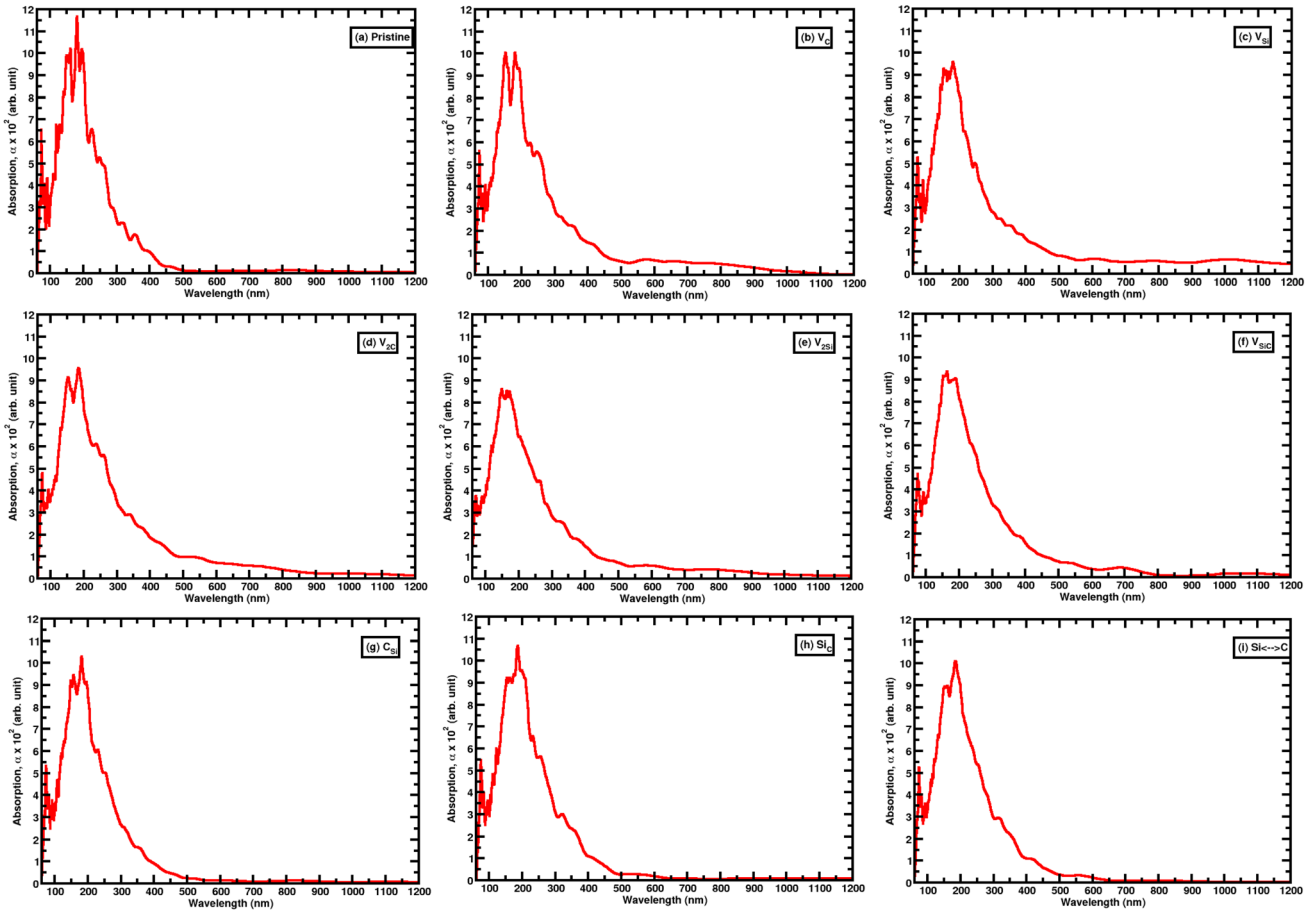

Fig. 13 (a) The absorption coefficient of pristine monolayer SiC; the absorption coefficient of single vacancy defect in a monolayer of SiC: (b) V_C, (c) V_{Si}; the absorption coefficient of double vacancy defect in a monolayer of SiC: (d) V_{2C}, (e) V_{2Si}, (f) V_{SiC}; the absorption coefficient of antisite defect in a monolayer of SiC: (g) C_{Si}, (h) Si_C, (i) Si ↔ C.

LED, it is necessary to obtain structures that are capable of emitting blue, green, and red light. Subsequently, we determined the specific active layer that is accountable for producing visible light in our proposed LED. We found these structures through analysis of the power spectral density curve. Following the examination of the power spectral density curve, we proceed to analyze the remaining attributes of our proposed LED, focusing solely on the structures accountable for emitting blue, green, and red light.

3.3.1 Power spectral density. At constant 5 V, power spectral density in TCAD was measured with respect to wavelength. The simulated emission spectra are not symmetrical; they have a wider low-energy tail and a sharper high-energy cutoff. This phenomenon is caused by using Lorentzian broadening in the optical model, as well as the energy-dependent joint density of states and the Fermi–Dirac carrier distribution. The likelihood of radiative recombination changes over the energy spectrum, which causes the spectral profile to be asymmetric. The observed asymmetry is in line with electroluminescence spectra seen in several light-emitting devices that use semiconductors.

Initially, the model created by pure SiC was employed as an active layer in our proposed device, and the corresponding power spectral density curve is depicted in Fig. 17(a). Fig. 17(a) indicates that the peak intensity occurs at a wavelength of 480 nm. Subsequently, a single antisite defect in SiC (C_{Si}) was employed as the active layer, with the peak power spectral density observed at 620 nm. Thereafter, a double antisite defect in SiC (Si ↔ C) was utilized as the active layer, exhibiting a maximum power spectral density intensity at 868 nm. Using In_{Si} as the active layer gave the highest power spectral density at 504 nm, which is close to green light. However, by utilizing Ca_{Si} as the active layer, we achieved the highest power spectral density at a wavelength of 534 nm, resulting in the emission of green light. We obtained the maximum power spectrum density at 628 nm and 613 nm, which emit near red light, when we employed As_{Si} and P_{Si} as the active layer, respectively. However, the maximum power spectral density, which is red light, was observed at 668 nm when K_{Si} was utilized as the active layer. Based on our power spectral density analysis as shown in Fig. 17(b), by using the pristine SiC, Ca_{Si}, and K_{Si} as an active layer of our proposed LED should be capable of producing blue, green, and red light, respectively.

3.3.2 Energy band and radiative recombination. The simulated band structure of the proposed LED, incorporating pristine SiC, K_{Si}, and Ca_{Si} as an active layer, has been analyzed under an applied input voltage of 5 V. The corresponding

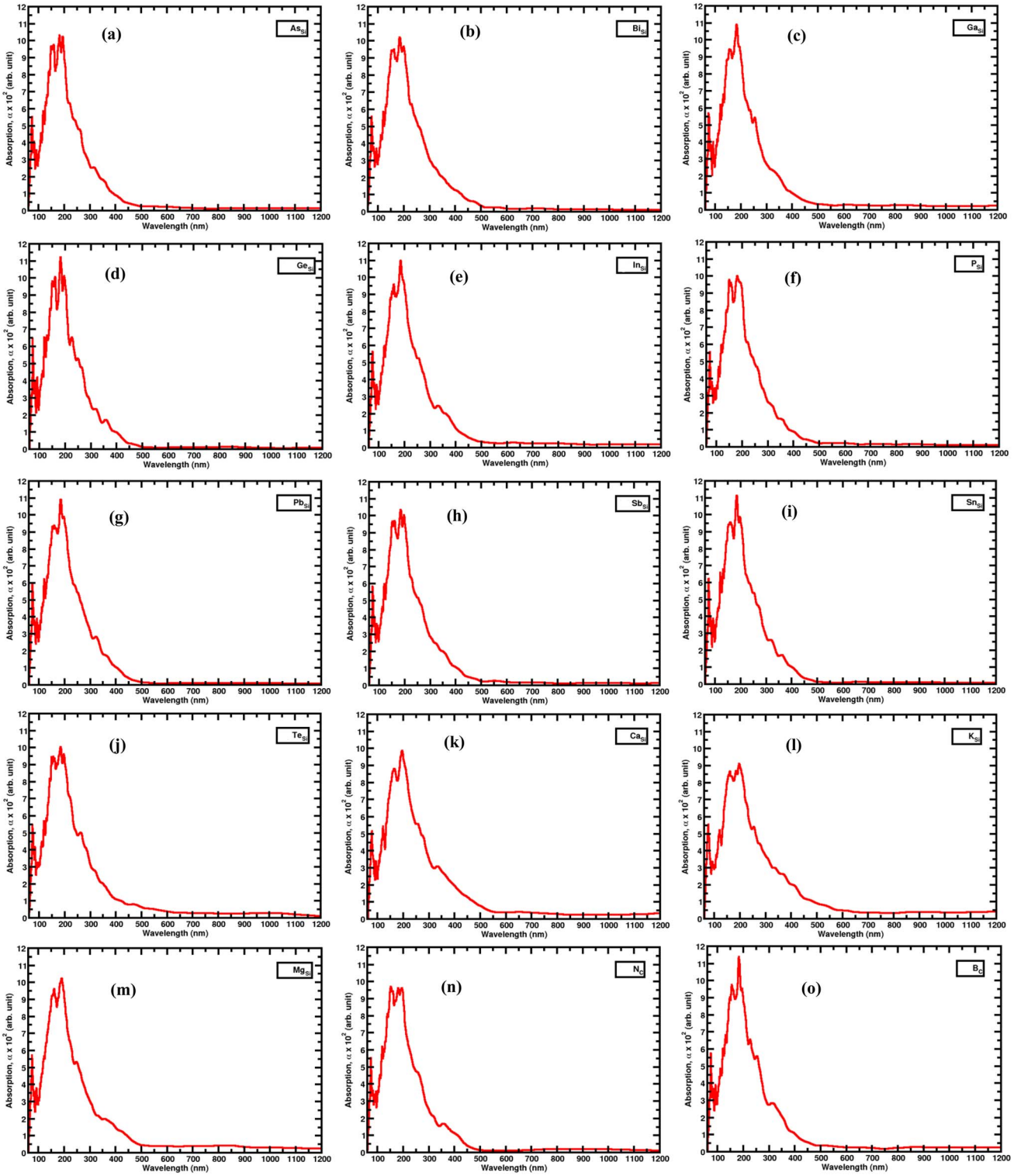

Fig. 14 The absorption coefficient of point doping in a monolayer of SiC: (a) As_{Si}, (b) Bi_{Si}, (c) Ga_{Si}, (d) Ge_{Si}, (e) In_{Si}, (f) P_{Si}, (g) Pb_{Si}, (h) Sb_{Si}, (i) Sn_{Si}, (j) Te_{Si}, (k) Ca_{Si}, (l) K_{Si}, (m) Mg_{Si}, (n) N_C, (o) B_C.

results are illustrated in Fig. 18(a). On the other hand, the radiative recombination rates for the proposed LED utilizing pristine SiC, K_{Si}, and Ca_{Si} are presented in Fig. 18(b).

3.3.3 IQE. Fig. 19(a) illustrates the internal quantum efficiency (IQE) of the proposed LED. The IQE characteristics depicted in Fig. 19(a) indicate that the pristine SiC-based LED exhibits the highest internal quantum efficiency among the three configurations. In contrast, the Ca_{Si} based LED shows a little reduced IQE, whereas the K_{Si} based LED shows the lowest IQE.

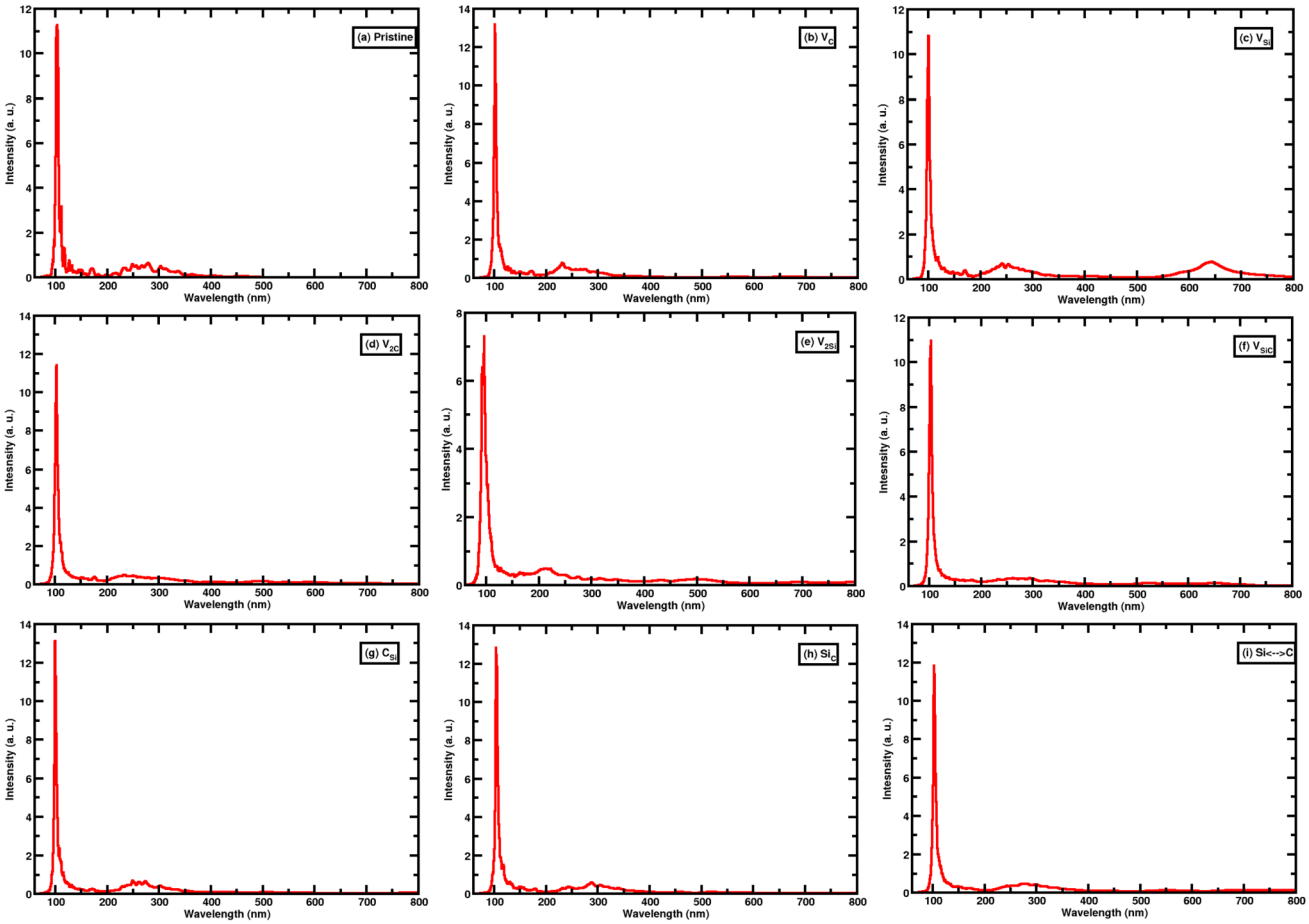

Fig. 15 (a) The electron energy loss spectrum of pristine monolayer SiC; the electron energy loss spectrum of single vacancy defect in a monolayer of SiC: (b) V_C, (c) V_{Si}; the electron energy loss spectrum of double vacancy defect in a monolayer of SiC: (d) V_{2C}, (e) V_{2Si}, (f) V_{SiC}; the electron energy loss spectrum of antisite defect in a monolayer of SiC: (g) C_{Si}, (h) Si_C, (i) Si ↔ C.

3.3.4 Light extraction efficiency. Each electron injected into the active region of an ideal LED results in the emission of a single photon. An electron, being a charged particle, produces a photon which is a particle of light. Photons generated within the active region must be able to escape the LED die. An ideal LED would achieve zero-loss extraction efficiency by emitting all of the photons generated in the active zone into space. However, in a practical LED, not all the power generated in the active region is emitted into the surrounding environment. The high refractive index of semiconductors contributes significantly to this reduced extraction efficiency.

The effectiveness of light extraction is characterized as:

$$\eta = \frac{\text{amount of photons released into space in a second}}{\text{amount of photons released from the active area in a second}}$$

$$\text{or,} \quad \eta = \frac{P_{\text{out}}/(h\nu)}{P_{\text{int}}/(h\nu)}$$

Here, P_{int} is the amount of light that the active area emits, and the optical power that is released into space is denoted as P_{out}. The simulation assumes that the structure is level and smooth and that the emission is directed straight out from the surface. The study didn't take into account things like waveguiding, substrate absorption, and surface roughness, which made the estimation of LEE too perfect. We got the optical constants for 4H-SiC, namely the refractive index (n) and the absorption coefficient (α), from well-known experimental data.[46,109,125] We used first-principles calculations in this study to find the optical constants for 2D-SiC.

The higher refractive index of materials within the active layer might result in light confinement, leading to the reabsorption of emitted photons. If the substrate can absorb light at the same wavelength as the emission, some of the emitted light may be reabsorbed by the substrate, thus degrading the overall efficiency and performance of the LED. Additionally, when light encounters a metallic contact surface, a portion of it may be absorbed by the metal. Furthermore, total internal reflection, often referred to as the trapped light phenomenon, further constrains the amount of light that can exit the semiconductor. Methods include adding layers with an intermediate refractive index or texturing the surface, which can help reduce these losses by increasing optical out-coupling.[126–128]

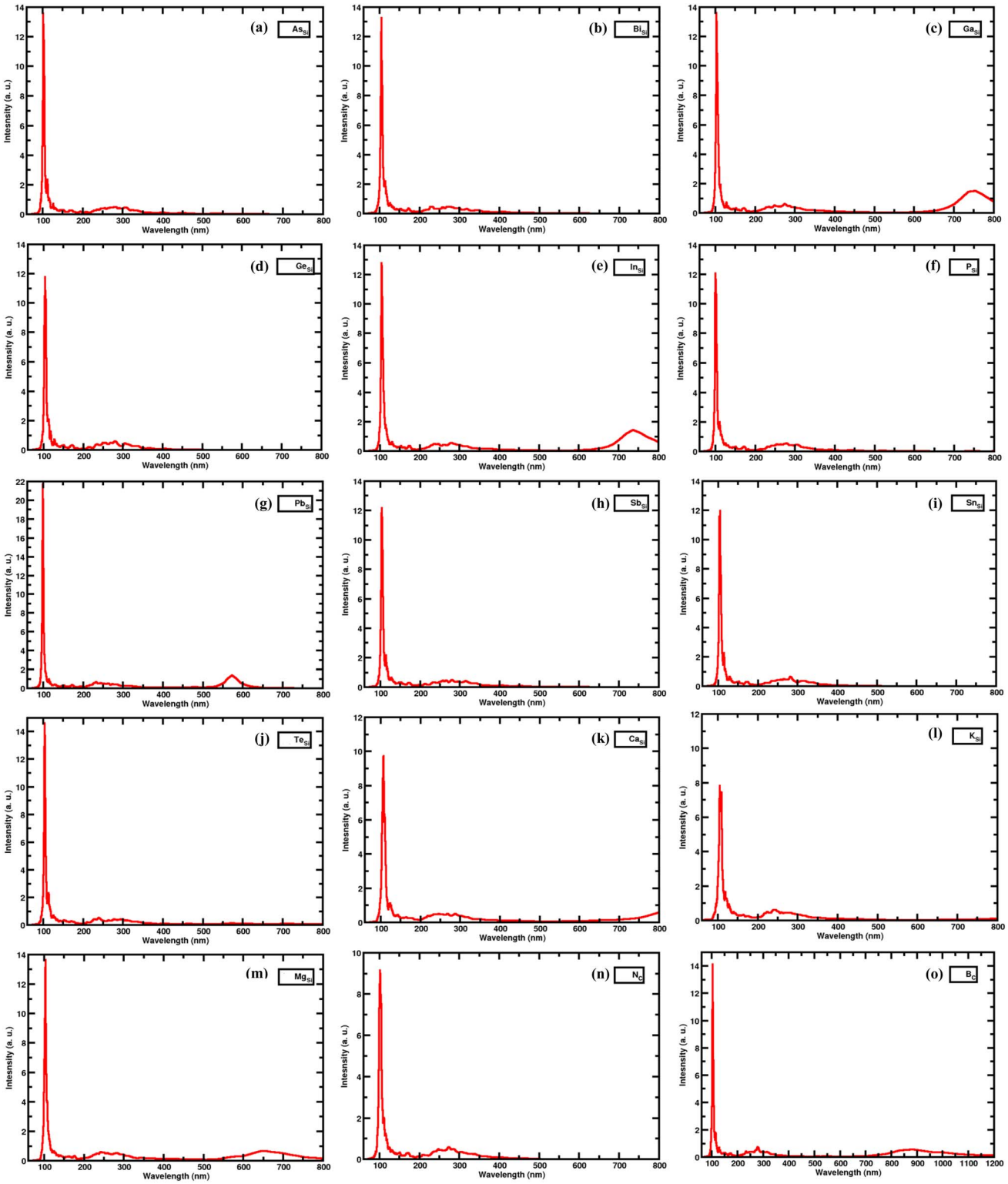

Fig. 16 The electron energy loss spectrum of point doping in a monolayer of SiC: (a) As_{Si}, (b) Bi_{Si}, (c) Ga_{Si}, (d) Ge_{Si}, (e) In_{Si}, (f) P_{Si}, (g) Pb_{Si}, (h) Sb_{Si}, (i) Sn_{Si}, (j) Te_{Si}, (k) Ca_{Si}, (l) K_{Si}, (m) Mg_{Si}, (n) N_C, (o) B_C.

Absorption and the imaginary component of the dielectric function (ε_2) also have a major impact on the LED structure's light extraction efficiency (LEE). An increase in the absorption coefficient inside the active region causes a decrease in LEE due to an increase in photon losses. In addition, absorption is directly affected by the imaginary component of the dielectric function (ε_2), with a greater ε_2 value indicating more absorption losses and reduced LEE. Therefore, in order to increase LEE in SiC-based

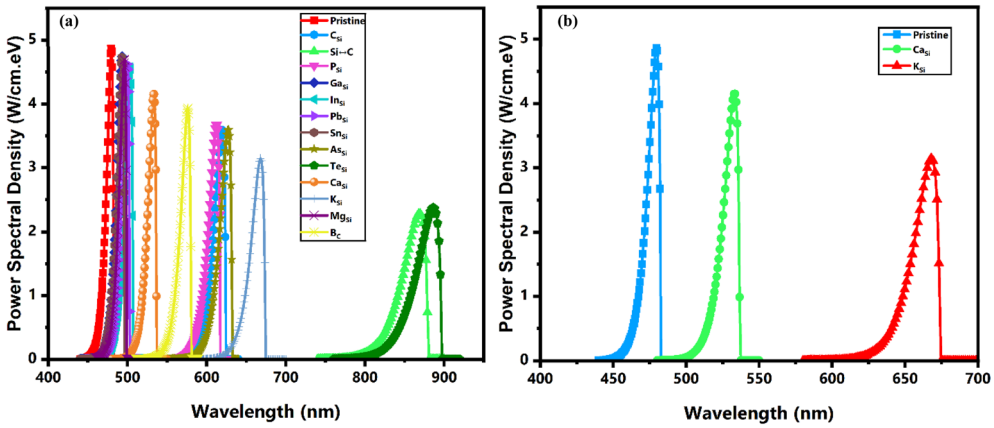

Fig. 17 (a) Power spectrum density as a function of wavelength for SiC-based LED; (b) the peak of the power spectral density is seen at 480 nm, 534 nm, and 668 nm, respectively. Here, the power spectrum density, which stands for the optical power emitted per unit area per unit energy interval, is represented in W cm^{-1} eV^{-1}.

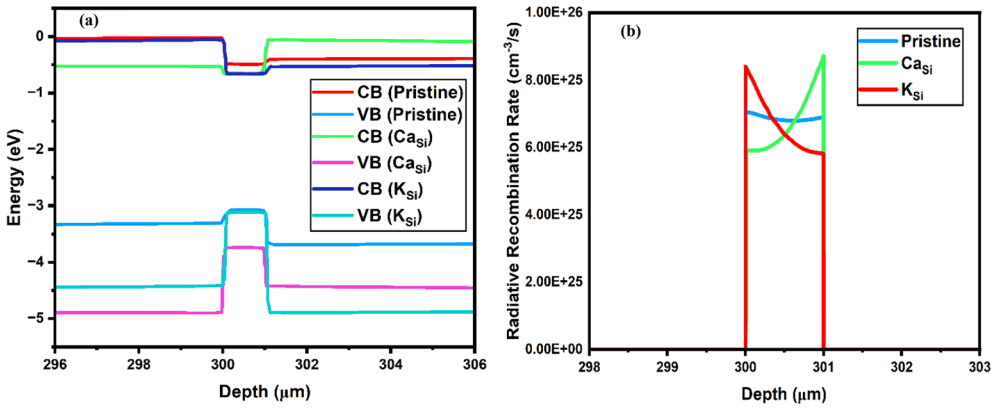

Fig. 18 (a) Energy band diagram of the proposed LED utilizing pristine SiC, K_{Si}, and Ca_{Si} as an active layer at an applied bias of 5 V; (b) radiative recombination characteristics of the proposed LED utilizing pristine SiC, K_{Si}, and Ca_{Si} as an active layer.

LEDs, it is vital to optimize the characteristics of the material in order to improved refractive index matching and obtain low absorption. The point doping approach significantly modifies the optical characteristics of materials, leading to decreased optical losses and a notable improvement in LEE relative to their pristine forms. After analyzing the optical properties of pristine SiC, K_{Si}, and Ca_{Si}, we can see that K_{Si} gives the best optical characteristics. This improvement indicates that K_{Si} is the most suitable candidate for optimizing LEE in the proposed LED configuration.

We determined the light extraction efficiency of our proposed structure as shown in Fig. 19(b). A fixed bias of 5 V is used in these computations for the simulated LED structure. Notably, the efficiency is only 10.27% when utilizing pristine SiC as the active layer. However, employing Ca_{Si} as an active layer results in a significant enhancement of our extraction efficiency, with an increase of 16.04%. When K_{Si} is used as the active layer, the extraction efficiency is doubled to a value of 22.57% compared to when pristine SiC is employed as the active layer.

The computed LEE values provide us an idea of how well different 2D-SiC layouts can radiate. In practice, these values can be increased even more by optimizing photonic structures. Dielectric mirror back reflectors, microlens arrays, graded-index encapsulation, and surface patterning are some of the ways to improve light outcoupling by reducing total internal reflection. Adding optical enhancements to future simulations and device fabrication will help us get a better idea of how much light can be extracted from real LED systems.

3.3.5 *I–V* characteristics. In our proposed LED configuration, we utilized pure 2D-SiC, Ca_{Si}, and K_{Si} as an active layer to examine their effects on the relationship between anode voltage and anode current density. The relevant outcomes are depicted in Fig. 20(a). Fig. 20(a) demonstrates that when utilizing pristine SiC, Ca_{Si}, and K_{Si} as the active layer, all exhibit nearly identical characteristics in terms of anode voltage *versus* anode current density. The current exhibits a higher value when pristine SiC is utilized as the active layer. Conversely, when we employ Ca_{Si} as the active layer, it exhibits a relatively lower current.

A little difference in current density is apparent based on the individual material utilized. When pristine 2D-SiC acts as the active layer, the device has the maximum current density over

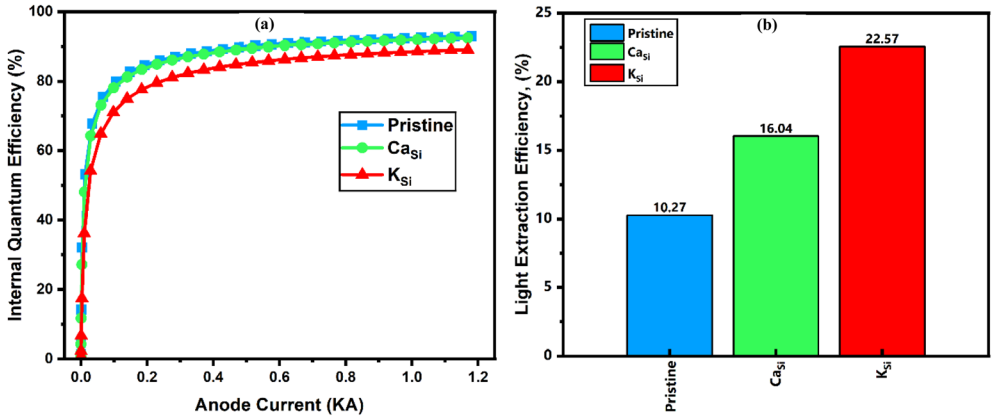

Fig. 19 (a) Variation of internal quantum efficiency as a function of anode current for the proposed LED utilizing pristine SiC, K_{Si}, and Ca_{Si} as an active layer; (b) the light extraction efficiency of proposed LEDs.

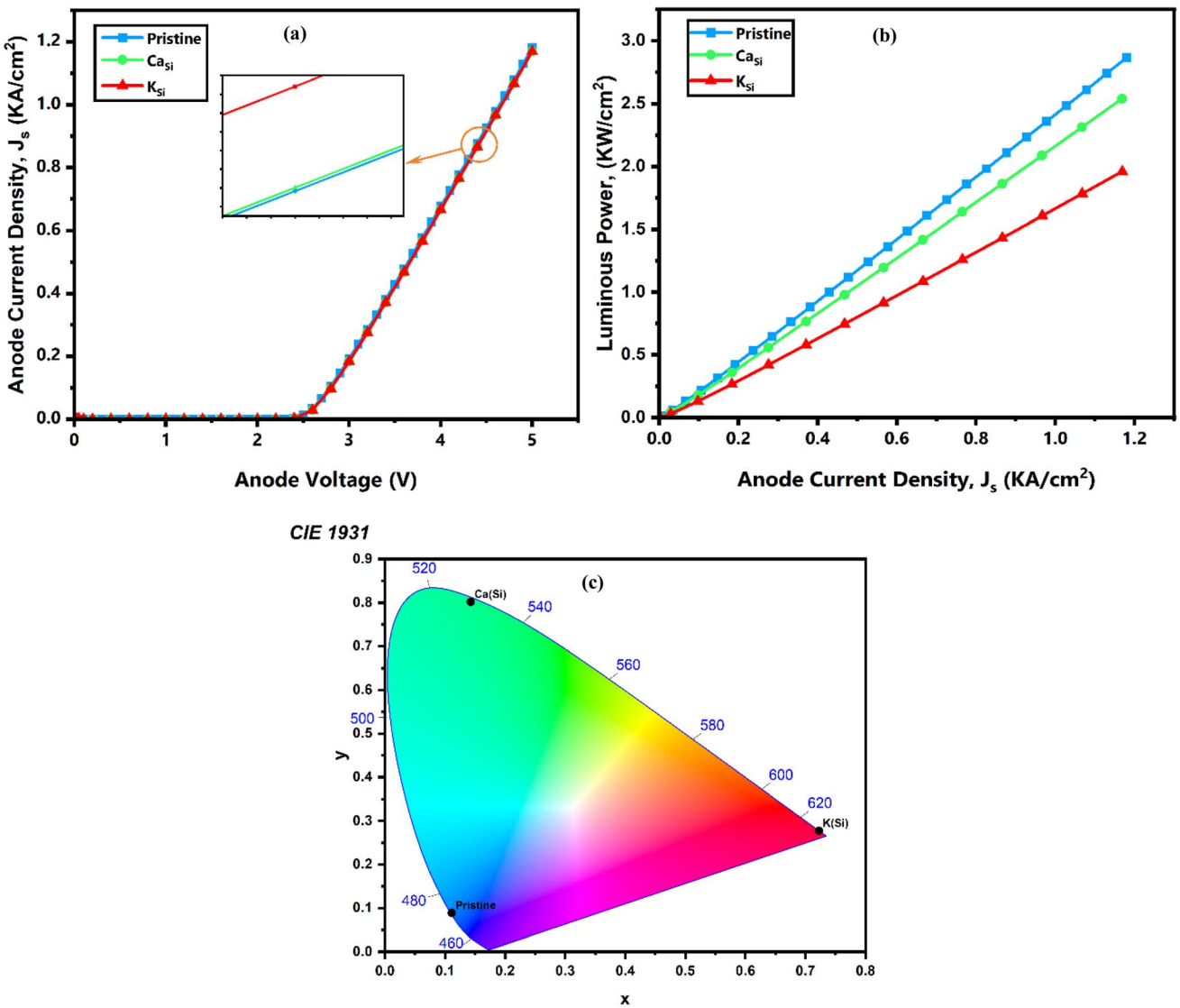

Fig. 20 (a) Anode voltage *versus* anode current density characteristics of the proposed SiC-based LED, illustrating its electrical behavior. (b) Relationship between current density and luminous power output, indicating the electroluminescent efficiency of the device. (c) CIE 1931 chromaticity diagram showing the emission color coordinates corresponding to different active layers, including pristine SiC, K_{Si}, and Ca_{Si}. The plot highlights the color tunability of the LED through specific dopant incorporation.

the examined voltage range. Conversely, substituting the active layer with Ca_{Si} yields a somewhat diminished current density, indicating a disparity in charge carrier transport qualities or interfacial features between the electrode and the active material. An intermediate level of current conduction is indicated by the behavior of K_{Si}, which is found to fall between these two scenarios.

3.3.6 Luminous power. An analysis has been conducted on the relationship between power output and anode current density in our suggested LED, while maintaining a fixed bias voltage of 5v. The active layer materials used in this analysis were pristine SiC, Ca_{Si}, and K_{Si}. To examine the luminous electric power of the LED, it is necessary to have information on the current density (J_s). The relationship between current density and the luminous power output is presented in Fig. 20(b). Fig. 20(b) shows that when pristine SiC is employed as the active layer in our suggested LED, the increase in luminous power is slightly higher compared to using K_{Si} or Ca_{Si}. However, compared to pristine SiC, Ca_{Si} used as the active layer in our proposed LED, the luminous power increases slightly less when K_{Si} is used.

3.3.7 CIE. The suggested LED structure utilizes pristine 2D-SiC as an active layer, resulting in light emission within the wavelength range of 440 nm to 485 nm. The emitted light exhibits a narrow line width and falls within the precise blue color region, as depicted in Fig. 20(c). On the other hand, the proposed LED design has a Ca_{Si} layer as the active material, which enables the emission of light in the wavelength range of 478 nm to 539 nm. The light that is produced has a very small range of wavelengths and is located specifically in the green portion of the electromagnetic spectrum, as seen in Fig. 20(c). By employing K_{Si} as an active layer, the proposed LED structure is able to emit light with a wavelength range of 580 nm to 674 nm. Fig. 20(c) shows that the emitted light has a short line width and is exactly in the red color area.

3.3.8 White LED combinations. The single and multichip types are the two primary categories that represent the fabrication technology of white LED at present.[62] We proposed a single-chip design in which the three monochromatic light radiations produced by the green, blue, and red LEDs are combined to produce white light, as seen in (Fig. 21). An inherent benefit is in the ability to modify the necessary light color to suit various requirements. In all the LEDs, we employed 2D SiC as the active layer. Specifically, we utilized pure 2D SiC for the blue LED, Ca_{Si} for the green LED, and K_{Si} for the red LED. The area size of each LED is determined by a thorough analysis of the power spectral density graph. Here, we alter the width to vary the area of the LED, but the length remains the same. The width of the red, green, and blue LED is represented by the W_R, W_G and W_B symbols, respectively. Our suggested LED chip has a width of 1 μm, with red, blue, and green LEDs having widths of 0.4, 0.34, and 0.26 μm, respectively (Fig. 21).

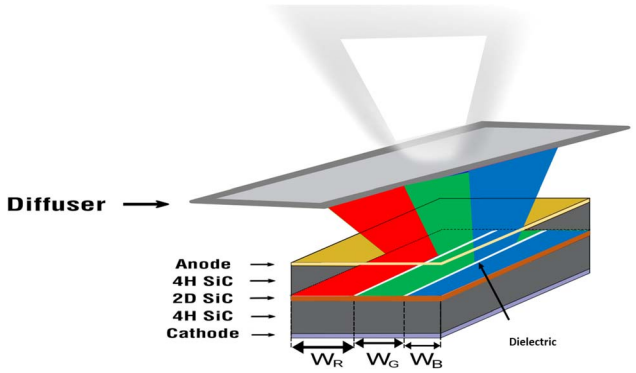

Fig. 21 A white LED device is a composite of red, green, and blue integrated LED chips, where W_R and W_G represent the width of the K_{Si} and Ca_{Si}, respectively, and W_B represents the width of the pristine 2D SiC as an active layer. Dielectric trenches (*e.g.*, SiO_2) provide lateral isolation. Each zone has a separate transparent top contact (*e.g.*, ITO), with a shared N-type bottom contact.

3.4 Roadmap for experimental implementation

The results of this study are based only on theoretical calculations, but improvements in the synthesis and characterization of materials make it possible to test these results in the real world. Researchers made monolayer 2D-SiC utilizing bottom-up methods including chemical vapor deposition (CVD) and solid-state reactions on SiO_2/Si and h-BN substrates.[49,51] Recent advances in both theory and experiment have made it much easier to understand and manage point defect and doping in two-dimensional materials used in electronics and optoelectronics. Da *et al.*[129] showed that it is possible to make freestanding monolayer SiC in graphene nanopores in a controlled way by using electron irradiation and *in situ* heating. This is a new way to build planar 2D heterostructures with atomic accuracy.[129] This study looks at many types of defects and dopants, including as vacancies, antisites, and substitutional atoms. These can be added to an experiment *via* focused ion beam (FIB) implantation, plasma exposure, or controlled chemical doping. These methods have been used in the past to make point-level changes in 2D materials with spatial accuracy.[130,131]

Yoo *et al.*[132] looked at a number of electrical doping methods for 2D semiconductors, including substitutional, chemical, and charge-transfer methods. These methods have worked well in materials like graphene and transition metal dichalcogenides (TMDs).[133] Wang *et al.*[134] came up with a modulation doping method that lets defects in nearby encapsulation layers provide or take free carriers. This makes it possible to do n- or p-type doping in 2D heterostructures without damaging them. Xu *et al.*[135] showed that high-energy ion implantation with a protective PMMA layer could dope 2D materials such as MoS_2 with phosphorus. This worked well for doping while causing less harm to the lattice structure.

Defect engineering is very important for controlling the flow of light and carriers. Chen *et al.*[136] found that adding group IIIA elements to 2D material such as WS_2 monolayers increases the quantum yield of photoluminescence and makes it easier to change the polarity of carriers. This helps make optoelectronic devices that work well and stay stable. Jiang *et al.*[90] say that methods like electron beam irradiation, plasma treatment, and

chemical doping make it easier to fine-tune defect patterns in 2D materials, which makes them work better.[137] Wang *et al.*[138] showed how to make ordered silicon vacancy arrays in SiC systems using a scalable, maskless focused ion beam approach. These arrays are photostable single-photon emitters that work better at lower doses. Telkhozhayeva and Girshevitz[139] looked at how the parameters of an ion beam and how it interacts with a substrate affect the production of defects in 2D materials. They came up with rules for making defects in a controlled and repeatable way.[140] Mohseni *et al.*[40] came up with a way to make SiC by employing aluminum precursors to make silicon vacancy and divacancy quantum defects directly. They changed the settings to increase the number of paramagnetic defects, which was confirmed by electron spin resonance studies.[141] Jin *et al.*[142] used cathodoluminescence to study silicon vacancies in 4H-SiC. This confirmed that these point defects are optically active.[138,143] At the same time, Beke and Gali[144] showed how to turn bulk SiC containing vacancies into nanoparticles, which is a process that can be used for quantum applications.

To check the chemical states of dopants and defects, X-ray photoelectron spectroscopy (XPS) is used to look at the structural and optical implications of these changes. Photoluminescence (PL) and Raman spectroscopy are good at finding changes in band structure and emissions caused by faults. High-resolution transmission electron microscopy (HRTEM) makes it possible to see lattice distortions and the quality of surfaces directly.[40,145] Doped 2D-SiC layers can be transferred onto conducting substrates or directly grown on wide-bandgap semiconductors such as GaN or 4H-SiC for device fabrication. It is possible to establish metal connections to create LED structures oriented either horizontally or vertically. Recent investigations on 2D-SiC's light-emitting applications show that current–voltage (*I–V*) analysis and electroluminescence (EL) measurements can be used to characterize these devices.[29,146,147]

The simulations assume perfect ohmic connections and don't take into account excitonic effects, temperature fluctuations, or interface trap states. Also, the defect modeling based on supercells uses defect densities that are higher than what is usually seen in experiments. Advanced simulations and experimental testing will look at these things in the future. The results of the computer simulations are very useful for guiding actual work on optoelectronic devices made of 2D-SiC with dopants and defects.

The proposed white LED has three individual LED placed on top of each other. Each one is responsible for giving off red, green, or blue light. The intrinsic portion of each LED has a single layer of 2D-SiC that is point doped to emit certain wavelengths: K-doped 2D-SiC for red, Ca-doped 2D-SiC for green, and pure 2D-SiC for blue. The P-type and N-type zones are made up of strongly doped 4H-SiC, which has carrier concentrations of about 1×10^{18} cm^{-3}. Ion implantation or *in situ* doping during epitaxial growth are the most common ways to reach doping levels.[109,148–151] Photolithography and dry etching are used to make dielectric trenches, like SiO_2, that separate the three emission zones. This is a common approach used in high-resolution LED arrays.[152–154] Selective area growth or transfer printing is used to make 2D-SiC monolayers, which lets the doped layers be arranged in space accurately.[155–161] Each LED unit has a top transparent electrode, like indium tin oxide (ITO) or graphene, and a bottom electrode that all pixels share. Graphene films or Ag nanowires are examples of current-spreading layers that can be used to make light emission more even and reduce resistive losses.[160,162,163] This setup makes it possible to put all three main emission colors on a single chip, which makes a small and adjustable white LED possible. The design uses fabrication methods that have already been used in the fields of 2D materials, micro-LEDs, and heterogeneous optoelectronics.

4 Conclusion

The recent experimental demonstration of monolayer 2D-SiC growth and advancements in 2D-3D heterostructure device fabrication show that the material systems and device concepts proposed in this study can be tested in the lab.[51,54,55,57,141] The fact that our theoretical results match up with recent events shows how important the proposed RGB white LED design is. It also shows how important it is for future study to keep using combined simulation-experiment methods. The primary objective of this study is to investigate the electrical and optical properties of two-dimensional silicon carbide (2D-SiC) under various structural configurations, including the pristine form, systems with antisite and vacancy defects, and doped with different foreign elements. Initially, we aim to identify which of the modified 2D-SiC retain a direct band gap upon the introduction of such defects or dopants. Our results show that pristine 2D-SiC possesses a direct band gap of 2.57 eV. Moreover, single atom doping in SiC, such as calcium (Ca) and potassium (K) preserves this direct band gap nature, indicating that controlled doping strategies can be employed to modulate the material's electronic properties, thus making it a promising candidate for optoelectronic applications, particularly in LEDs. To further explore the device-level performance, we utilized the SILVACO TCAD platform to conduct the simulations of LED structures incorporating 2D-SiC in pristine, defective, and doped forms. The simulation results confirm that the designed LEDs are capable of emitting light across the visible spectrum, specifically in the blue, green, and red regions, thereby enabling the generation of white light. Among the configurations studied, the LED based on pristine SiC exhibits the highest luminous intensity and maximum power spectral density. In contrast, the K_{Si} LED demonstrates the highest light extraction efficiency (LEE), underscoring its potential for improved optical output in practical applications.

Ethical approval

All the writers said that the article does not have research on human topics, human components, tissues, or organisms.

Author contributions

Md. Mahfuzul Haque: writing – review & editing, writing – original draft, visualization, validation, software, resources,

methodology, investigation, formal analysis, data curation, conceptualization. Sajid Muhaimin Choudhury: writing – review & redact, writing – original draft, visualization, validation, supervision, software, resources, methodology, investigation, formal analysis, data curation, conceptualization.

Conflicts of interest

All the writers said that they have no acquaintances. There are no competitional pecuniary interests, or private relations relationships that could influence the research reported in this article.

Data availability

Data for this article, including electrical, optical, device data are available at Zenodo at **https://doi.org/10.5281/zenodo.15749900**.

Acknowledgements

I express my sincere gratitude to my thesis supervisor Dr Sajid Muhaimin Choudhury Sir, who has always supported me at every stage of the research with guidance, encouragement and constructive feedback. Without his leadership and professionalism, this work would not have been possible.

References

1 A. K. Geim and K. S. Novoselov, The rise of graphene, *Nat. Mater.*, 2007, **6**(3), 183–191, DOI: **10.1038/NMAT1849;KWRD=MATERIALS+SCIENCE**.

2 B. Partoens and F. M. Peeters, From graphene to graphite: Electronic structure around the K point, *Phys. Rev. B: Condens. Matter Mater. Phys.*, 2006, **74**(7), 075404, DOI: **10.1103/PHYSREVB.74.075404/FIGURES/11/THUMBNAIL**.

3 A. Bostwick, J. McChesney, T. Ohta, E. Rotenberg, T. Seyller and K. Horn, Experimental studies of the electronic structure of graphene, *Prog. Surf. Sci.*, 2009, **84**(11–12), 380–413, DOI: **10.1016/J.PROGSURF.2009.08.002**.

4 H. Wei, *et al.*, Stability and thermoelectric performance of the two-dimensional rare-earth compounds RTeCl (R=La,Pr,Nd), *Phys. Rev. Appl.*, 2024, **21**(5), 054026, DOI: **10.1103/PHYSREVAPPLIED.21.054026/FIGURES/7/THUMBNAIL**.

5 S. Z. Butler, *et al.*, Progress, challenges, and opportunities in two-dimensional materials beyond graphene, *ACS Nano*, 2013, **7**(4), 2898–2926, DOI: **10.1021/NN400280C/ASSET/IMAGES/MEDIUM/NN-2013-00280C_0018.GIF**.

6 Q. H. Wang, K. Kalantar-Zadeh, A. Kis, J. N. Coleman and M. S. Strano, Electronics and optoelectronics of two-dimensional transition metal dichalcogenides, *Nat. Nanotechnol.*, 2012, **7**(11), 699–712, DOI: **10.1038/NNANO.2012.193;SUBJMETA=1018,1130,357,639,766,925,995;KWRD=ELECTRONIC+PROPERTIES+AND+MATERIALS,ELECTRONICS**.

7 K. F. Mak and J. Shan, Photonics and optoelectronics of 2D semiconductor transition metal dichalcogenides, *Nat. Photonics*, 2016, **10**(4), 216–226, DOI: **10.1038/NPHOTON.2015.282;SUBJMETA=1019,1021,1054,301,399,624,639,918;KWRD=NANOPHOTONICS+AND+PLASMONICS,OPTICAL+PROPERTIES+AND+DEVICES**.

8 F. Schedin, *et al.*, Detection of individual gas molecules adsorbed on graphene, *Nat. Mater.*, 2007, **6**(9), 652–655, DOI: **10.1038/NMAT1967;KWRD=MATERIALS+SCIENCE**.

9 B. Liu and K. Zhou, Recent progress on graphene-analogous 2D nanomaterials: properties, modeling and applications, *Prog. Mater. Sci.*, 2019, **100**, 99–169, DOI: **10.1016/j.pmatsci.2018.09.004**.

10 N. R. Glavin, *et al.*, Emerging Applications of Elemental 2D Materials, *Adv. Mater.*, 2020, **32**(7), 1904302, DOI: **10.1002/ADMA.201904302;JOURNAL:JOURNAL:15214095;PAGEGROUP:STRING:PUBLICATION**.

11 S. V. Morozov, *et al.*, Giant intrinsic carrier mobilities in graphene and its bilayer, *Phys. Rev. Lett.*, 2008, **100**(1), 016602, DOI: **10.1103/PHYSREVLETT.100.016602/FIGURES/4/THUMBNAIL**.

12 A. C. Ferrari, *et al.*, Raman spectrum of graphene and graphene layers, *Phys. Rev. Lett.*, 2006, **97**(18), 187401, DOI: **10.1103/PHYSREVLETT.97.187401/FIGURES/3/THUMBNAIL**.

13 K. S. Novoselov, *et al.*, Two-dimensional gas of massless Dirac fermions in graphene, *Nature*, 2005, **438**(7065), 197–200, DOI: **10.1038/NATURE04233;KWRD=SCIENCE**.

14 E. Bekyarova, M. E. Itkis, P. Ramesh and R. C. Haddon, Chemical approach to the realization of electronic devices in epitaxial graphene, *Phys. Status Solidi RRL*, 2009, **3**(6), 184–186, DOI: **10.1002/PSSR.200903110**.

15 J. Gebhardt, *et al.*, Growth and electronic structure of boron-doped graphene, *Phys. Rev. B: Condens. Matter Mater. Phys.*, 2013, **87**(15), 155437, DOI: **10.1103/PHYSREVB.87.155437/FIGURES/5/THUMBNAIL**.

16 B. Verberck, B. Partoens, F. M. Peeters and B. Trauzettel, Strain-induced band gaps in bilayer graphene, *Phys. Rev. B: Condens. Matter Mater. Phys.*, 2012, **85**(12), 125403, DOI: **10.1103/PHYSREVB.85.125403/FIGURES/4/THUMBNAIL**.

17 J. Lee, K. A. Min, S. Hong and G. Kim, Ab initio study of adsorption properties of hazardous organic molecules on graphene: Phenol, phenyl azide, and phenylnitrene, *Chem. Phys. Lett.*, 2015, **618**, 57–62, DOI: **10.1016/J.CPLETT.2014.10.064**.

18 C. Xu, P. A. Brown, J. Lu and K. L. Shuford, Electronic Properties of Halogen-Adsorbed Graphene, *J. Phys. Chem. C*, 2015, **119**(30), 17271–17277, DOI: **10.1021/ACS.JPCC.5B05595/SUPPL_FILE/JP5B05595_SI_001.PDF**.

19 V. Krasnenko, J. Kikas and M. G. Brik, Modification of the structural and electronic properties of graphene by the benzene molecule adsorption, *Phys. B*, 2012, **407**(23), 4557–4561, DOI: **10.1016/J.PHYSB.2012.08.019**.

20 M. Tayyab, A. Hussain, W. Adil, S. Nabi and Q. u. A. Asif, Band-gap engineering of graphene by Al doping and

adsorption of Be and Br on impurity: A computational study, *Comput. Condens. Matter*, 2020, **23**, e00463, DOI: 10.1016/J.COCOM.2020.E00463.

21 T. Yu, Z. Ni, C. Du, Y. You, Y. Wang and Z. Shen, Raman mapping investigation of graphene on transparent flexible substrate: The strain effect, *J. Phys. Chem. C*, 2008, **112**(33), 12602–12605, DOI: 10.1021/JP806045U/ASSET/IMAGES/MEDIUM/JP-2008-06045U_0005.GIF.

22 C. Si, Z. Sun and F. Liu, Strain engineering of graphene: a review, *Nanoscale*, 2016, **8**(6), 3207–3217, DOI: 10.1039/C5NR07755A.

23 P. A. Denis, C. Pereyra Huelmo and A. S. Martins, Band Gap Opening in Dual-Doped Monolayer Graphene, *J. Phys. Chem. C*, 2016, **120**(13), 7103–7112, DOI: 10.1021/ACS.JPCC.5B11709/ASSET/IMAGES/MEDIUM/JP-2015-117092_0015.GIF.

24 M. M. Haque, M. R. Islam and S. M. Choudhury, Investigation of the physical properties through strain effect of monolayer silicon carbide material: DFT analysis, *Phys. B*, 2025, **697**, 416670, DOI: 10.1016/J.PHYSB.2024.416670.

25 H. Shu and J. Guo, Enhanced stability and tunable optoelectronic properties of silicon–carbon monolayers by strain and surface functionalization, *J. Mater. Chem. C*, 2024, **12**(16), 5916–5925, DOI: 10.1039/D4TC00401A.

26 T. Sultan, J. Islam and Md. M. Hassan, Mechanical Behaviors of the Single Crystal Two-Dimensional Silicon Carbide (SiC): A Molecular Dynamics Insight, *Malays. J. Compos. Sci. Manuf.*, 2023, **12**(1), 102–113, DOI: 10.37934/MJCSM.12.1.102113.

27 A. S. M. J. Islam, M. S. Islam, N. Ferdous, J. Park and A. Hashimoto, Vacancy-induced thermal transport in two-dimensional silicon carbide: a reverse non-equilibrium molecular dynamics study, *Phys. Chem. Chem. Phys.*, 2020, **22**(24), 13592–13602, DOI: 10.1039/D0CP00990C.

28 M. M. Haque and S. M. Choudhury, DFT Analysis of Strain Effect in Bilayer 2D-SiC on Electrical, Optical, Phonon, and Thermodynamic Properties, *2024 13th International Conference on Electrical and Computer Engineering (ICECE)*, 2024, pp. 206–211, DOI: 10.1109/ICECE64886.2024.11024753.

29 S. Chabi, Z. Guler, A. J. Brearley, A. D. Benavidez and T. S. Luk, The creation of true two-dimensional silicon carbide, *Nanomaterials*, 2021, **11**(7), 1799, DOI: 10.3390/NANO11071799/S1.

30 T. Susi, *et al.*, Computational insights and the observation of SiC nanograin assembly: towards 2D silicon carbide, *Sci. Rep.*, 2017, **7**(1), 1–9, DOI: 10.1038/s41598-017-04683-9.

31 C. L. Freeman, F. Claeyssens, N. L. Allan and J. H. Harding, Graphitic nanofilms as precursors to eurtzite gilms: Theory, *Phys. Rev. Lett.*, 2006, **96**(6), 066102, DOI: 10.1103/PHYSREVLETT.96.066102/FIGURES/3/THUMBNAIL.

32 P. Tsipas, *et al.*, Evidence for graphite-like hexagonal AlN nanosheets epitaxially grown on single crystal Ag(111), *Appl. Phys. Lett.*, 2013, **103**(25), DOI: 10.1063/1.4851239/26060.

33 C. Noguera and J. Goniakowski, Polarity in oxide ultrathin films, *J. Phys.: Condens. Matter*, 2008, **20**(26), 264003, DOI: 10.1088/0953-8984/20/26/264003.

34 J. Goniakowski, L. Giordano and C. Noguera, Polarity of ultrathin MgO(111) films deposited on a metal substrate, *Phys. Rev. B: Condens. Matter Mater. Phys.*, 2010, **81**(20), 205404, DOI: 10.1103/PHYSREVB.81.205404/FIGURES/7/THUMBNAIL.

35 X. Liu, Z. Zhang, Z. Luo, B. Lv and Z. Ding, Tunable Electronic Properties of Graphene/g-AlN Heterostructure: The Effect of Vacancy and Strain Engineering, *Nanomaterials*, 2019, **9**(12), 1674, DOI: 10.3390/NANO9121674.

36 W. X. Zhang, T. Li, S. B. Gong, C. He and L. Duan, Tuning the electronic and magnetic properties of graphene-like AlN nanosheets by surface functionalization and thickness, *Phys. Chem. Chem. Phys.*, 2015, **17**(16), 10919–10924, DOI: 10.1039/C5CP00123D.

37 E. F. de Almeida, A. Kakanakova-Georgieva and G. K. Gueorguiev, On Decorating a Honeycomb AlN Monolayer with Hydrogen and Fluorine Atoms: *Ab Initio* and Experimental Aspects, *Materials*, 2024, **17**(3), 616, DOI: 10.3390/MA17030616.

38 M. Singh, *et al.*, Defect-Free, Few-Atomic-Layer Thin ZnO Nanosheets with Superior Excitonic Properties for Optoelectronic Devices, *ACS Nano*, 2024, **18**(26), 16947–16957, DOI: 10.1021/ACSNANO.4C03098/SUPPL_FILE/NN4C03098_SI_001.PDF.

39 R. Morales-Salvador, I. Demiroglu, F. Viñes and S. T. Bromley, Tuning the electronic properties of ZnO nanofilms *via* strain-induced structural phase transformations and quantum confinement, *Nanoscale*, 2025, **17**(14), 8764–8777, DOI: 10.1039/D4NR05206D.

40 M. Mohseni, *et al.*, Vacancy-related color centers in two-dimensional silicon carbide monolayers, *Phys. Rev. Mater.*, 2024, **8**(5), 056201, DOI: 10.1103/PHYSREVMATERIALS.8.056201/FIGURES/6/THUMBNAIL.

41 G. Zhang, Y. Cheng, J. P. Chou and A. Gali, Material platforms for defect qubits and single-photon emitters, *Appl. Phys. Rev.*, 2020, **7**(3), DOI: 10.1063/5.0006075/123998.

42 C. R. Eddy and D. K. Gaskill, Silicon Carbide as a Platform for Power Electronics, *Science*, 2009, **324**(5933), 1398–1400, DOI: 10.1126/SCIENCE.1168704.

43 S. Castelletto, *et al.*, A silicon carbide room-temperature single-photon source, *Nat. Mater.*, 2014, **13**(2), 151–156, DOI: 10.1038/NMAT3806;SUBJMETA=1000,1019,119,301,482,639;KWRD=QUANTUM+OPTICS,SEMICONDUCTORS.

44 S. Chabi and K. Kadel, Two-Dimensional Silicon Carbide: Emerging Direct Band Gap Semiconductor, *Nanomaterials*, 2020, **10**(11), 2226, DOI: 10.3390/NANO10112226.

45 H. Şahin, *et al.*, Monolayer honeycomb structures of group-IV elements and III-V binary compounds: First-principles calculations, *Phys. Rev. B: Condens. Matter Mater. Phys.*, 2009, **80**(15), 155453, DOI: 10.1103/PHYSREVB.80.155453/FIGURES/7/THUMBNAIL.

46 W. J. Choyke, H. Matsunami and G. Pensl, *Silicon Carbide: Recent Major Advances (Advanced Texts in Physics) (v. 79)*, Springer, https://books.google.com/books/about/Silicon_Carbide.html?id=mLBmKotEe9cC, accessed: May 30, 2025.

47 A. Singh, V. Mahamiya and A. Shukla, Defect-driven tunable electronic and optical properties of two-dimensional silicon carbide, *Phys. Rev. B*, 2023, **108**(23), 235311, DOI: 10.1103/PHYSREVB.108.235311/FIGURES/10/MEDIUM.

48 S. Lin, *et al.*, Quasi-Two-Dimensional SiC and SiC2: Interaction of Silicon and Carbon at Atomic Thin Lattice Plane, *J. Phys. Chem. C*, 2015, **119**(34), 19772–19779, DOI: 10.1021/ACS.JPCC.5B04113/SUPPL_FILE/JP5B04113_SI_001.PDF.

49 S. Chabi, H. Chang, Y. Xia and Y. Zhu, From graphene to silicon carbide: ultrathin silicon carbide flakes, *Nanotechnology*, 2016, **27**(7), 075602, DOI: 10.1088/0957-4484/27/7/075602.

50 X. Yang, R. Liu, B. Liu and M. Liu, Synthesis of Ultra-Thin Two-Dimensional SiC Using the CVD Method, *Energies*, 2022, **15**(17), 6351, DOI: 10.3390/EN15176351.

51 C. M. Polley, *et al.*, Bottom-Up Growth of Monolayer Honeycomb SiC, *Phys. Rev. Lett.*, 2023, **130**(7), 076203, DOI: 10.1103/PHYSREVLETT.130.076203/SUPPLEMENTALMATERIAL.PDF.

52 E. Ikonen, Recent advances and perspectives in photometry in the era of LED lighting, *Meas. Sci. Technol.*, 2023, **35**(2), 021001, DOI: 10.1088/1361-6501/AD0DE6.

53 I. Capan, Defects in Silicon Carbide as Quantum Qubits: Recent Advances in Defect Engineering, *Appl. Sci.*, 2025, **15**(10), 5606, DOI: 10.3390/app15105606.

54 S. H. Choi, Y. Kim, I. Jeon and H. Kim, Heterogeneous Integration of Wide Bandgap Semiconductors and 2D Materials: Processes, Applications, and Perspectives, *Adv. Mater.*, 2025, **37**(12), 2411108, DOI: 10.1002/ADMA.202411108;WEBSITE:WEBSITE:ADVANCED;CTYPE:STRING:JOURNAL.

55 X. Huang, C. Liu and P. Zhou, 2D semiconductors for specific electronic applications: from device to system, *npj 2D Mater. Appl.*, 2022, **6**(1), 1–19, DOI: 10.1038/s41699-022-00327-3.

56 F. Roccaforte, P. Fiorenza, M. Vivona, G. Greco and F. Giannazzo, Selective Doping in Silicon Carbide Power Devices, *Materials*, 2021, **14**(14), 3923, DOI: 10.3390/MA14143923.

57 L. Zhang and Z. Cui, First-Principles Study of Metal Impurities in Silicon Carbide: Structural, Magnetic, and Electronic Properties, *Front. Mater.*, 2022, **9**, 956675, DOI: 10.3389/FMATS.2022.956675/BIBTEX.

58 F. Bertoldo, S. Ali, S. Manti and K. S. Thygesen, Quantum point defects in 2D materials - the QPOD database, *npj Comput. Mater.*, 2022, **8**(1), 1–16, DOI: 10.1038/S41524-022-00730-W;SUBJMETA=1034,1038,119,301,639,766,995;KWRD=CONDENSED-MATTER+PHYSICS,ELECTRONIC+PROPERTIES+AND+MATERIALS,ELECTRONIC+STRUCTURE,THEORY+AND+COMPUTATION.

59 X. He, T. He, Z. Wang and M. Zhao, Neutral vacancy-defect-induced magnetism in SiC monolayer, *Phys. E*, 2010, **42**(9), 2451–2454, DOI: 10.1016/J.PHYSE.2010.06.010.

60 M. Bezi Javan, Electronic and magnetic properties of monolayer SiC sheet doped with 3d-transition metals, *J. Magn. Magn. Mater.*, 2016, **401**, 656–661, DOI: 10.1016/J.JMMM.2015.10.103.

61 G. A. Q. Abdulrahman, A. Aziz, N. A. A. Qasem and A. Alazzam, 2D Materials: Synthesis, properties, and energy-related applications, *Coord. Chem. Rev.*, 2025, **544**, 216950, DOI: 10.1016/J.CCR.2025.216950.

62 Y. Zhu, X. Sun, Y. Tang, L. Fu and Y. Lu, Two-dimensional materials for light emitting applications: Achievement, challenge and future perspectives, *Nano Res.*, 2021, **14**(6), 1912–1936, DOI: 10.1007/S12274-020-3126-9/METRICS.

63 Q. H. Wang, K. Kalantar-Zadeh, A. Kis, J. N. Coleman and M. S. Strano, Electronics and optoelectronics of two-dimensional transition metal dichalcogenides, *Nat. Nanotechnol.*, 2012, **7**(11), 699–712, DOI: 10.1038/nnano.2012.193.

64 Y. Yu, *et al.*, Dynamic Tuning of Single-Photon Emission in Monolayer WSe_2 *via* Localized Strain Engineering, *Nano Lett.*, 2025, **25**(9), 3438–3444, DOI: 10.1021/ACS.NANOLETT.4C05450/SUPPL_FILE/NL4C05450_SI_001.PDF.

65 Y. Sheng, T. Chen, Y. Lu, R. J. Chang, S. Sinha and J. H. Warner, High-Performance WS_2 Monolayer Light-Emitting Tunneling Devices Using 2D Materials Grown by Chemical Vapor Deposition, *ACS Nano*, 2019, **13**(4), 4530–4537, DOI: 10.1021/ACSNANO.9B00211/SUPPL_FILE/NN9B00211_SI_002.AVI.

66 S. S. K. Mallineni, *et al.*, Defect Engineered 2D Materials for Energy Applications, *Two-dimensional Materials - Synthesis, Characterization and Potential Applications*, 2016, DOI: 10.5772/64605.

67 F. Liu and Z. Fan, Defect engineering of two-dimensional materials for advanced energy conversion and storage, *Chem. Soc. Rev.*, 2023, **52**(5), 1723–1772, DOI: 10.1039/D2CS00931E.

68 Y. Liu, Z. Gao, Y. Tan and F. Chen, Enhancement of Out-of-Plane Charge Transport in a Vertically Stacked Two-Dimensional Heterostructure Using Point Defects, *ACS Nano*, 2018, **12**(10), 10529–10536, DOI: 10.1021/ACSNANO.8B06503/SUPPL_FILE/NN8B06503_SI_001.PDF.

69 S. Aftab, M. Z. Iqbal and M. W. Iqbal, Programmable Photo-Induced Doping in 2D Materials, *Adv. Mater. Interfaces*, 2022, **9**(32), 2201219, DOI: 10.1002/ADMI.202201219.

70 Y. Zhou, *et al.*, Improved Charge Injection and Transport of Light-Emitting Diodes Based on Two-Dimensional Materials, *Appl. Sci.*, 2019, **9**(19), 4140, DOI: 10.3390/APP9194140.

71 M. S. Islam, M. R. H. Mojumder, A. Hassan, M. U. Sohag, and J. Park, High-Efficiency Multi Quantum Well Blue LED Using 2D-SiC as an Active Material, *2021 5th International Conference on Electrical Engineering and Information and Communication Technology, ICEEICT 2021*, 2021, DOI: 10.1109/ICEEICT53905.2021.9667843.

72 M. H. Rashid, A. Koel, T. Rang, N. Nasir, H. Mehmood and S. Cheema, Modeling and Simulations of 4H-SiC/6H-SiC/4H-SiC Single Quantum-Well Light Emitting Diode Using Diffusion Bonding Technique, *Micromachines*, 2021, **12**(12), 1499, DOI: 10.3390/MI12121499.

73 M. Cerezo, *et al.*, Variational quantum algorithms, *Nat. Rev. Phys.*, 2021, **3**(9), 625–644, DOI: 10.1038/s42254-021-00348-9.

74 W. Kohn and L. J. Sham, Self-consistent equations including exchange and correlation effects, *Phys. Rev.*, 1965, **140**(4A), A1133, DOI: 10.1103/PHYSREV.140.A1133/FIGURE/1/THUMB.

75 J. P. Perdew, K. Burke and M. Ernzerhof, Generalized Gradient Approximation Made Simple, *Phys. Rev. Lett.*, 1996, **77**(18), 3865, DOI: 10.1103/PhysRevLett.77.3865.

76 M. E. Casida and M. Huix-Rotllant, Progress in time-dependent density-functional theory, *Annu. Rev. Phys. Chem.*, 2012, **63**, 287–323, DOI: 10.1146/ANNUREV-PHYSCHEM-032511-143803/CITE/REFWORKS.

77 P. Giannozzi, *et al.*, QUANTUM ESPRESSO: a modular and open-source software project for quantumsimulations of materials, *J. Phys.: Condens. Matter*, 2009, **21**(39), 395502, DOI: 10.1088/0953-8984/21/39/395502.

78 L. Pan, *et al.*, First-principles study of monolayer and bilayer honeycomb structures of group-IV elements and their binary compounds, *Phys. Lett. A*, 2011, **375**(3), 614–619, DOI: 10.1016/J.PHYSLETA.2010.11.062.

79 P. Giannozzi, *et al.*, QUANTUM ESPRESSO: A modular and open-source software project for quantum simulations of materials, *J. Phys.: Condens. Matter*, 2009, **21**(39), 395502, DOI: 10.1088/0953-8984/21/39/395502.

80 H. J. Monkhorst and J. D. Pack, Special points for Brillouin-zone integrations, *Phys. Rev. B*, 1976, **13**(12), 5188, DOI: 10.1103/PhysRevB.13.5188.

81 H. P. Komsa and A. V. Krasheninnikov, Effects of confinement and environment on the electronic structure and exciton binding energy of MoS2 from first principles, *Phys. Rev. B: Condens. Matter Mater. Phys.*, 2012, **86**(24), 241201, DOI: 10.1103/PHYSREVB.86.241201/FIGURES/3/THUMBNAIL.

82 M. B. Tagani, Si9 C15 monolayer: A silicon carbide allotrope with remarkable physical properties, *Phys. Rev. B*, 2023, **107**(8), 085114, DOI: 10.1103/PHYSREVB.107.085114/FIGURES/9/MEDIUM.

83 Z. Y. Gao, *et al.*, Experimental Realization of Atomic Monolayer Si9C15, *Adv. Mater.*, 2022, **34**(35), 2204779, DOI: 10.1002/ADMA.202204779;WEBSITE:WEBSITE:ADVANCED;CTYPE:STRING:JOURNAL.

84 H. Lee, K. Paeng and I. S. Kim, A review of doping modulation in graphene, *Synth. Met.*, 2018, **244**, 36–47, DOI: 10.1016/J.SYNTHMET.2018.07.001.

85 T. O. Wehling, *et al.*, Molecular doping of graphene, *Nano Lett.*, 2008, **8**(1), 173–177, DOI: 10.1021/NL072364W.

86 S. K. Saha, R. C. Chandrakanth, H. R. Krishnamurthy and U. V. Waghmare, Mechanisms of molecular doping of graphene: A first-principles study, *Phys. Rev. B: Condens. Matter Mater. Phys.*, 2009, **80**(15), 155414, DOI: 10.1103/PHYSREVB.80.155414/FIGURES/5/THUMBNAIL.

87 D. Dumcenco, *et al.*, Large-area epitaxial monolayer moS2, *ACS Nano*, 2015, **9**(4), 4611–4620, DOI: 10.1021/ACSNANO.5B01281/SUPPL_FILE/NN5B01281_SI_001.PDF.

88 B. Sachs, *et al.*, Doping mechanisms in graphene-MoS2 hybrids, *Appl. Phys. Lett.*, 2013, **103**(25), DOI: 10.1063/1.4852615/25854.

89 M. N. Bui, *et al.*, Low-energy Se ion implantation in MoS_2 monolayers, *npj 2D Mater. Appl.*, 2022, **6**(1), 1–8, DOI: 10.1038/S41699-022-00318-4;SUBJMETA=1000,1018,1032,119,639,766,925,930;KWRD=DESIGN.

90 J. Jiang, T. Xu, J. Lu, L. Sun and Z. Ni, Defect Engineering in 2D Materials: Precise Manipulation and Improved Functionalities, *Research*, 2019, **2019**, 4641739, DOI: 10.34133/2019/4641739.

91 G. Litrico, M. Zimbone, L. Calcagno, P. Musumeci, G. A. Baratta and G. Fotil, Point defects induced in ion irradiated 4H-SiC probed by exciton lines, *Nucl. Instrum. Methods Phys. Res., Sect. B*, 2009, **267**(8–9), 1243–1246, DOI: 10.1016/J.NIMB.2009.01.147.

92 L. Guo, *et al.*, Accurate Measurement of Defect Generation Rates in Silicon Carbide Irradiated with Energetic Ions, *ACS Omega*, 2023, **8**(44), 41977–41982, DOI: 10.1021/ACSOMEGA.3C07568/ASSET/IMAGES/LARGE/AO3C07568_0004.JPEG.

93 J. Hong, *et al.*, Exploring atomic defects in molybdenum disulphide monolayers, *Nat. Commun.*, 2015, **6**(1), 1–8, DOI: 10.1038/ncomms7293.

94 T. Susi, J. Kotakoski, D. Kepaptsoglou, C. Mangler, T. C. Lovejoy, O. L. Krivanek and R. Zan, Silicon–carbon bond inversions driven by 60-keV electrons in graphene, *Phys. Rev. Lett.*, 2014, **113**(11), 115501, DOI: 10.1103/PhysRevLett.113.115501.

95 V. Khemka, R. Patel, N. Ramungul, T. P. Chow, M. Ghezzo and J. Kretchmer, Characterization of phosphorus implantation in 4H-SiC, *J. Electron. Mater.*, 1999, **28**(3), 167–174, DOI: 10.1007/S11664-999-0008-Z/METRICS.

96 R. Nipoti, *et al.*, High-dose phosphorus-implanted 4H-SiC: Microwave and conventional post-implantation annealing at temperatures ≥1700 °C, *J. Electron. Mater.*, 2012, **41**(3), 457–465, DOI: 10.1007/S11664-011-1794-7/METRICS.

97 S. Porcar, J. González, D. Fraga, T. Stoyanova Lyubenova, G. Soraca and J. B. Carda, Effect of Al, Ga, and In Doping on the Optical, Structural, and Electric Properties of ZnO Thin Films, *Appl. Sci.*, 2021, **11**(21), 10122, DOI: 10.3390/APP112110122.

98 E. T. Seid and F. B. Dejene, Gallium and indium co-doping effects on structural, optical and luminescence properties of ZnO nanostructures, *Mater. Today Commun.*, 2021, **27**, 102330, DOI: 10.1016/J.MTCOMM.2021.102330.

99 J. Zhang, *et al.*, Ultra-wide bandgap semiconductor Ga_2O_3 power diodes, *Nat. Commun.*, 2022, **13**(1), 1–8, DOI: 10.1038/S41467-022-31664-Y;TECHMETA=120,128;SUBJMETA=1005,1007,166,301,639,987;KWRD=ELECTRICAL+

AND+ELECTRONIC+ENGINEERING, ELECTRONIC+DEVICES.

100 J. L. Lyons, D. Wickramaratne and A. Janotti, Dopants and defects in ultra-wide bandgap semiconductors, *Curr. Opin. Solid State Mater. Sci.*, 2024, **30**, 101148, DOI: 10.1016/J.COSSMS.2024.101148.

101 M. F. Hossen, S. Shendokar and S. Aravamudhan, Defects and Defect Engineering of Two-Dimensional Transition Metal Dichalcogenide (2D TMDC) Materials, *Nanomaterials*, 2024, **14**(5), 410, DOI: 10.3390/NANO14050410.

102 Q. Zhang, A. T. S. Wee, Q. Liang, X. Zhao and M. Liu, Defect engineering of two-dimensional transition-metal dichalcogenides: Applications, challenges, and opportunities, *ACS Nano*, 2021, **15**(2), 2165–2181, DOI: 10.1021/ACSNANO.0C09666/ASSET/IMAGES/MEDIUM/NN0C09666_0013.GIF.

103 V. A. Fedorov, S. A. Kozlov, N. A. Potolokov and S. V. Nikolashin, Preparation of high-purity gallium from semiconductor fabrication waste, *Inorg. Mater.*, 2006, **42**(SUPPL. 1), S70–S89, DOI: 10.1134/S0020168506130048/METRICS.

104 W. Cai, *et al.*, A state-of-the-art review on solid-state metal joining, *J. Manuf. Sci. Eng.*, 2019, **141**(3), 031012, DOI: 10.1115/1.4041182/369169.

105 R. Rusnaldy, Diffusion bonding: an advanced of material process, *Rotasi*, 2001, **3**(1), 23–27, DOI: 10.14710/ROTASI.3.1.23-27, https://ejournal.undip.ac.id/index.php/rotasi/article/view/2487/2199.

106 T. Kimoto and Y. Yonezawa, Current status and perspectives of ultrahigh-voltage SiC power devices, *Mater. Sci. Semicond. Process.*, 2018, **78**, 43–56, DOI: 10.1016/J.MSSP.2017.10.010.

107 G. Ferro, New Approaches to *In Situ* Doping of SiC Epitaxial Layers, *Adv. Mater. Res.*, 2011, **324**, 14–19, DOI: 10.4028/WWW.SCIENTIFIC.NET/AMR.324.14.

108 Z. Tang, *et al.*, Study on the Surface Structure of N-Doped 4H-SiC Homoepitaxial Layer Dependence on the Growth Temperature and C/Si Ratio Deposited by CVD, *Crystals*, 2023, **13**(2), 193, DOI: 10.3390/CRYST13020193.

109 T. Kimoto and J. A. Cooper, *Fundamentals of Silicon Carbide Technology: Growth, Characterization, Devices and Applications*, 2014, vol. 9781118313527, pp. 1–538, DOI: 10.1002/9781118313534.

110 S. Ji, *et al.*, The growth of low resistivity, heavily Al-doped 4H-SiC thick epilayers by hot-wall chemical vapor deposition, *J. Cryst. Growth*, 2013, **380**, 85–92, DOI: 10.1016/J.JCRYSGRO.2013.05.039.

111 U. Forsberg, Ö. Danielsson, A. Henry, M. K. Linnarsson and E. Janzén, Aluminum doping of epitaxial silicon carbide, *J. Cryst. Growth*, 2003, **253**(1–4), 340–350, DOI: 10.1016/S0022-0248(03)01045-5.

112 D. M. Caughey and R. E. Thomas, Carrier Mobilities in Silicon Empirically Related to Doping and Field, *Proc. IEEE*, 1967, **55**(12), 2192–2193, DOI: 10.1109/PROC.1967.6123.

113 S. Selberherr, Process and device modeling for VISI, *Microelectron. Reliab.*, 1984, **24**(2), 225–257, DOI: 10.1016/0026-2714(84)90450-5.

114 M. Grundmann, *The Physics of Semiconductors*, 2016, DOI: 10.1007/978-3-319-23880-7.

115 H. C. Hsueh, G. Y. Guo and S. G. Louie, Excitonic effects in the optical properties of a SiC sheet and nanotubes, *Phys. Rev. B: Condens. Matter Mater. Phys.*, 2011, **84**(8), 085404, DOI: 10.1103/PHYSREVB.84.085404/FIGURES/9/MEDIUM.

116 G. J. Snyder and E. S. Toberer, Complex thermoelectric materials, *Nat. Mater.*, 2008, **7**(2), 105–114, DOI: 10.1038/NMAT2090;KWRD=MATERIALS+SCIENCE.

117 W. Liu, X. Yan, G. Chen and Z. Ren, Recent advances in thermoelectric nanocomposites, *Nano Energy*, 2012, **1**(1), 42–56, DOI: 10.1016/J.NANOEN.2011.10.001.

118 K. F. Brennan, *The Physics of Semiconductors*, 1999, https://ui.adsabs.harvard.edu/abs/1999phse.book.....B/abstract, accessed: Jun. 12, 2025.

119 C. Zhang, R. Wang, H. Mishra and Y. Liu, Two-Dimensional Semiconductors with High Intrinsic Carrier Mobility at Room Temperature, *Phys. Rev. Lett.*, 2023, **130**(8), 087001, DOI: 10.1103/PhysRevLett.130.087001.

120 S. H. Mir, V. K. Yadav, J. K. Singh and J. K. Singh, Recent Advances in the Carrier Mobility of Two-Dimensional Materials: A Theoretical Perspective, *ACS Omega*, 2020, **5**(24), 14203–14211, DOI: 10.1021/ACSOMEGA.0C01676/ASSET/IMAGES/LARGE/AO0C01676_0003.JPEG.

121 L. Cheng, C. Zhang and Y. Liu, Intrinsic charge carrier mobility of 2D semiconductors, *Comput. Mater. Sci.*, 2021, **194**, 110468, DOI: 10.1016/J.COMMATSCI.2021.110468.

122 J. S. Park and H. J. Choi, Band-gap opening in graphene: A reverse-engineering approach, *Phys. Rev. B: Condens. Matter Mater. Phys.*, 2015, **92**(4), 045402, DOI: 10.1103/PHYSREVB.92.045402/FIGURES/6/THUMBNAIL.

123 Z. H. Ni, T. Yu, Y. H. Lu, Y. Y. Wang, Y. P. Feng and Z. X. Shen, Uniaxial strain on graphene: Raman spectroscopy study and band-gap opening, *ACS Nano*, 2008, **2**(11), 2301–2305, DOI: 10.1021/NN800459E/ASSET/IMAGES/MEDIUM/NN-2008-00459E_0006.GIF.

124 K. Nassau, *Colour*, http://https://www.britannica.com/science/color.

125 K. Sun, *et al.*, Synthesis and potential applications of silicon carbide nanomaterials/nanocomposites, *Ceram. Int.*, 2022, **48**(22), 32571–32587, DOI: 10.1016/J.CERAMINT.2022.07.204.

126 A. R. Anwar, M. T. Sajjad, M. A. Johar, C. A. Hernández-Gutiérrez, M. Usman and S. P. Łepkowski, Recent Progress in Micro-LED-Based Display Technologies, *Laser Photonics Rev.*, 2022, **16**(6), 2100427, DOI: 10.1002/LPOR.202100427;PAGE:STRING:ARTICLE/CHAPTER.

127 A. Pandey, M. Reddeppa, Z. Mi, A. Pandey, M. Reddeppa and Z. Mi, Recent progress on micro-LEDs, *Light: Adv. Manuf.*, 2024, **4**(4), 519–542, DOI: 10.37188/LAM.2023.031.

128 A. I. Zhmakin, Enhancement of light extraction from light emitting diodes, *Phys. Rep.*, 2011, **498**(4–5), 189–241, DOI: 10.1016/J.PHYSREP.2010.11.001.

129 Y. Da, *et al.*, Controlled fabrication of freestanding monolayer SiC by electron irradiation, *Chin. Phys. B*, 2024, **33**(8), 086802, DOI: 10.1088/1674-1056/AD6132.
130 M. Schleberger and J. Kotakoski, 2D Material Science: Defect Engineering by Particle Irradiation, *Materials*, 2018, **11**(10), 1885, DOI: 10.3390/MA11101885.
131 M. Heilmann, V. Deinhart, A. Tahraoui, K. Höflich and J. M. J. Lopes, Spatially controlled epitaxial growth of 2D heterostructures *via* defect engineering using a focused He ion beam, *npj 2D Mater. Appl.*, 2021, **5**(1), 1–7, DOI: 10.1038/s41699-021-00250-z.
132 H. Yoo, K. Heo, M. H. R. Ansari and S. Cho, Recent advances in electrical doping of 2d semiconductor materials: Methods, analyses and applications, *Nanomaterials*, 2021, **11**(4), 832, DOI: 10.3390/NANO11040832.
133 D. Gupta and R. Kumar, Ion implantation as an approach for tuning of electronic structure, optical, morphological and electrical transport properties of sputtered molybdenum disulfide thin films, *Mater. Sci. Semicond. Process.*, 2023, **158**, 107326, DOI: 10.1016/J.MSSP.2023.107326.
134 D. Wang, X. Bin Li and H. B. Sun, Modulation Doping: A Strategy for 2D Materials Electronics, *Nano Lett.*, 2021, **21**(14), 6298–6303, DOI: 10.1021/ACS.NANOLETT.1C02192/SUPPL_FILE/NL1C02192_SI_001.PDF.
135 K. Xu, *et al.*, Doping of two-dimensional MoS2 by high energy ion implantation, *Semicond. Sci. Technol.*, 2017, **32**(12), 124002, DOI: 10.1088/1361-6641/AA8ED3.
136 Y. Chen, *et al.*, Defect Engineering of 2D Semiconductors for Dual Control of Emission and Carrier Polarity, *Adv. Mater.*, 2024, **36**(14), 2312425, DOI: 10.1002/ADMA.202312425;PAGE:STRING:ARTICLE/CHAPTER.
137 Y. Zhou, X. Shi and Y. Zhang, Defect and its inverse problems in 1D and 2D materials, *Mater. Sci. Eng., B*, 2024, **307**, 117516, DOI: 10.1016/J.MSEB.2024.117516.
138 J. Wang, *et al.*, Scalable fabrication of single silicon vacancy defect arrays in silicon carbide using focused ion beam, *ACS Photonics*, 2017, **4**(5), 1054–1059, DOI: 10.1021/acsphotonics.7b00230.
139 M. Telkhozhayeva and O. Girshevitz, Roadmap toward Controlled Ion Beam-Induced Defects in 2D Materials, *Adv. Funct. Mater.*, 2024, **34**(45), 2404615, DOI: 10.1002/ADFM.202404615.
140 D. Wang, X. Bin Li, D. Han, W. Q. Tian and H. B. Sun, Engineering two-dimensional electronics by semiconductor defects, *Nano Today*, 2017, **16**, 30–45, DOI: 10.1016/J.NANTOD.2017.07.001.
141 M. W. Yu, *et al.*, Role of defects in the photoluminescence and photoresponse of WS_2–graphene heterodevices, *Appl. Surf. Sci.*, 2024, **642**, 158541, DOI: 10.1016/J.APSUSC.2023.158541.
142 Y. Jin, *et al.*, Photoluminescence spectra of point defects in semiconductors: Validation of first-principles calculations, *Phys. Rev. Mater.*, 2021, **5**(8), 084603, DOI: 10.1103/PHYSREVMATERIALS.5.084603/FIGURES/8/THUMBNAIL.
143 M. Mohseni, I. A. Sarsari, S. Karbasizadeh, P. Udvarhelyi, Q. Hassanzade, T. Ala-Nissila and A. Gali, Vacancy-related color centers in two-dimensional silicon carbide monolayers, *Phys. Rev. Mater.*, 2024, **8**(5), 056201, DOI: 10.1103/PhysRevMaterials.8.056201.
144 D. Beke and Á. Gali, "Method for preparation of point defects (vacancy) in silicon carbide particles, *European Pat.*, EP 3 770 114 A1, 2021, https://data.epo.org/publication-server/rest/v1.2/publication-dates/20210127/patents/EP3770114NWA1/document.pdf, accessed: Jul. 27, 2025.
145 H. Nan, *et al.*, Strong Photoluminescence Enhancement of MoS_2 through Defect Engineering and Oxygen Bonding, *ACS Nano*, 2014, **8**(6), 5738–5745, DOI: 10.1021/nn500532f.
146 S. Schwarz, *et al.*, Electrically pumped single-defect light emitters in WSe_2, *2D Mater.*, 2016, **3**(2), 025038, DOI: 10.1088/2053-1583/3/2/025038.
147 B. Schuler, *et al.*, Electrically driven photon emission from individual atomic defects in monolayer WS_2, *Sci. Adv.*, 2020, **6**(38), eabb5988, DOI: 10.1126/SCIADV.ABB5988.
148 K. Hwang, *et al.*, 1.6-Inch Transparent Micro-Display with Pixel Circuit Integrated microLED Chip Array by Misalignment-Free Transfer, *Adv. Mater.*, 2025, **37**(9), 2416015, DOI: 10.1002/ADMA.202416015;WEBSITE:WEBSITE:ADVANCED;CTYPE:STRING:JOURNAL.
149 J. Pernot, *et al.*, Control of Al-implantation doping in 4H-SiC, *Mater. Sci. Eng., B*, 2001, **80**(1–3), 362–365, DOI: 10.1016/S0921-5107(00)00601-2.
150 S. Das, D. J. Lichtenwalner, H. Dixit, S. Rogers, A. Scholze and S. H. Ryu, Study of Dopant Activation and Ionization for Phosphorus in 4H-SiC, *J. Electron. Mater.*, 2024, **53**(6), 2806–2810, DOI: 10.1007/S11664-024-10976-3/METRICS.
151 Y. Negoro, T. Kimoto, H. Matsunami, F. Schmid and G. Pensl, Electrical activation of high-concentration aluminum implanted in 4H-SiC, *J. Appl. Phys.*, 2004, **96**(9), 4916–4922, DOI: 10.1063/1.1796518.
152 X. Zou, Y. Cai, W. C. Chong and K. M. Lau, Fabrication and Characterization of High-Voltage LEDs Using Photoresist-Filled-Trench Technique, *J. Disp. Technol.*, 2016, **12**(4), 397–401, DOI: 10.1109/JDT.2015.2493368.
153 C. Kang, *et al.*, Fabrication of a vertically-stacked passive-matrix micro-LED array structure for a dual color display, *Opt. Express*, 2017, **25**(3), 2489–2495, DOI: 10.1364/OE.25.002489.
154 X. Zhang, W. Cheung Chong and K. May Lau, 848 ppi high-brightness active-matrix micro-LED micro-display using GaN-on-Si epi-wafers towards mass production, *Opt. Express*, 2021, **29**(7), 10580, DOI: 10.1364/OE.419877.
155 A. Chaves, *et al.*, Bandgap engineering of two-dimensional semiconductor materials, *npj 2D Mater. Appl.*, 2020, **4**(1), 1–21, DOI: 10.1038/s41699-020-00162-4.
156 B. Corbett, R. Loi, W. Zhou, D. Liu and Z. Ma, Transfer print techniques for heterogeneous integration of photonic components, *Prog. Quantum Electron.*, 2017, **52**, 1–17, DOI: 10.1016/J.PQUANTELEC.2017.01.001.

157 P. V. Pham, *et al.*, Transfer of 2D Films: From Imperfection to Perfection, *ACS Nano*, 2024, **18**(23), 14841–14876, DOI: 10.1021/ACSNANO.4C00590/ASSET/IMAGES/LARGE/NN4C00590_0023.JPEG.

158 I. Shahbaz, M. Tahir, L. Li and Y. Song, Advancements in 2D transition metal dichalcogenides (TMDs) inks for printed optoelectronics: A comprehensive review, *Mater. Today*, 2024, **77**, 142–184, DOI: 10.1016/J.MATTOD.2024.06.008.

159 Z. Cheng, *et al.*, Integrated optoelectronics with two-dimensional materials, *Natl. Sci. Open*, 2022, **1**(3), 20220022, DOI: 10.1360/NSO/20220022.

160 Y. Fu, *et al.*, Monolithic Integrated Device of GaN Micro-LED with Graphene Transparent Electrode and Graphene Active-Matrix Driving Transistor, *Materials*, 2019, **12**(3), 428, DOI: 10.3390/MA12030428.

161 G. Xue, B. Qin, C. Ma, P. Yin, C. Liu and K. Liu, Large-Area Epitaxial Growth of Transition Metal Dichalcogenides, *Chem. Rev.*, 2024, **124**(17), 9785–9865, DOI: 10.1021/ACS.CHEMREV.3C00851/ASSET/IMAGES/MEDIUM/CR3C00851_0031.GIF.

162 M. Oh, W. Y. Jin, H. Jun Jeong, M. S. Jeong, J. W. Kang and H. Kim, Silver Nanowire Transparent Conductive Electrodes for High-Efficiency III-Nitride Light-Emitting Diodes, *Sci. Rep.*, 2015, **5**(1), 1–11, DOI: 10.1038/SREP13483;SUBJMETA=1016,1020,1089,357,624,639,925;KWRD=INORGANIC+LEDS,NANOWIRES.

163 J. S. Park, *et al.*, Ag nanowire-based electrodes for improving the output power of ultraviolet AlGaN-based light-emitting diodes, *J. Alloys Compd.*, 2017, **703**, 198–203, DOI: 10.1016/J.JALLCOM.2017.01.351.